**Experimental Analysis of Dampened Breathing
Mode Oscillation on Hall Thruster Performance**

THESIS

Christopher D Vineski, Capt, USAF

AFIT-ENY-13-M-39
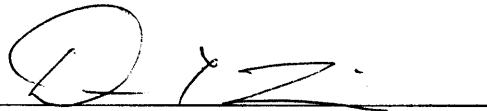
AFIT-ENY-13-M-39

EXPERIMENTAL ANALYSIS OF DAMPENED BREATHING MODE OSCILLATION ON HALL EFFECT THRUSTER PERFORMANCE

Christopher D Vineski, B.S.
Capt, USAF

Approved:

Capt. D. Liu Chairman	_13 Mar 2013_ Date
Dr. W. Bailey Member	_13 Mar 2013_ Date
Dr. W. Hargus Member	_13 Mar 2013_ Date
Dr. C. Hartsfield Member	_13 Mar 2013_ Date

AFIT-ENY-13-M-39

Abstract

Experiments were performed at the Air Force Institute of Technology to determine the effect of active control of the magnetic field strength to reduce the breathing mode oscillation on the efficiency of a 200 W Hall thruster. The breathing mode oscillation amplitude was measured by the root mean square (RMS) variation in the alternating current (AC) portion of the discharge current. The thruster was configured to run with either xenon or krypton propellant and experiments were performed with both propellants. Using the xenon propellant active control of the discharge RMS improved the propellant utilization efficiency by approximately 2% in two cases, while reducing the magnet current efficiency by approximately 10%. Active control of the discharge RMS's effect on the divergence angle of the thrust plume of the xenon thruster was unable to be determined due to large error. The overall effect was to decrease the total efficiency by approximately 5%. Using krypton propellant, the effect of active control of the discharge RMS on the propellant utilization was unable to be determined due to error. Active control of the RMS decreased the magnet current efficiency by approximately 11%. The divergence angle of the krypton was reduced by approximately 3°, resulting in an overall decrease in the total efficiency with krypton of approximately 6%. Overall, utilizing this method of reducing the breathing mode oscillation can be useful in satellites whose payload requires more power than the Hall thruster, as those satellites would be able to take advantage of the increase in propellant utilization efficiency or plume divergence without exceeding power capabilities.

Acknowledgements

Table of Contents

List of Figures

List of Tables

EXPERIMENTAL ANALYSIS OF DAMPENED BREATHING MODE
OSCILLATION ON HALL EFFECT THRUSTER PERFORMANCE

I. Introduction

1.1 Motivation

The objective of this effort is to quantify the effects of actively managing the
magnetic field strength, via the magnet current, on the efficiency and performance
of a 200 W Hall thruster. The current is managed to reduce the amplitude of the
Hall thruster's breathing mode oscillation. There is speculation that the oscillations
seen in the Hall thruster may contribute to the wearing of the wall lining insulator,
and hence is a life limiting factor of the Hall thruster [31, p. 190-191]. By reducing
these oscillations it is may be possible to improve the lifetime while maintaining
optimal thruster performance. Additionally, the study of Hall thrusters operating in
off-optimal conditions allows for satellite engineers and mission planners to have more
options for matching Hall thrusters to the design of specific spacecraft and missions.
This optimization will increase the payload capability of launched satellites, providing
expanded capabilities for the same cost. These improvements are especially important
during times of tight budgetary constraints.

1.2 History of Hall Thrusters

The history of electric space propulsion started at nearly the same time as the
development of rocket propulsion. Konstantin Tsiolkovsky, who developed the ideal
rocket equation, stated that "it is possible that in time we may use electricity to

produce a large velocity for the particles ejected from a rocket device [42, p. 95]" in 1911 [11]. Another great from the history of rocketry, Robert Goddard, was a visionary in the field of electric propulsion. In 1917, Goddard filed for a patent of the first documented electrostatic ion accelerator for propulsion purposes [15]. These visionaries advanced the concept of electric propulsion until the basic science was able to show its validity.

Electric propulsion was a lesser priority to rocket propulsion throughout the early stages of space exploration history. It was not until March of 1949 when L. R. Shepherd and A. V. Cleaver published the first quantitative analysis of the feasibility of electrostatic propulsion [39]. Unfortunately, their analysis included an attempt at 0.01 times gravity for the acceleration, which produced an enormous power plant requirement. Thus they concluded electric propulsion is not feasible. Fortunately for the community, Lyman Spitzer did a similar study two years later utilizing a more realistic acceleration, about 3.4×10^{-4} times gravity, showing electric propulsion is a viable technology [40]. Most of the early history of electric propulsion focused on electrostatic thrusters similar in concept to the modern ion engine [11].

Hall Thruster conceptualization and development began in the early 1960's with papers by Seikel and Reshotko, as well as Salz, Lary, et al. in the 1962 Bulletin of the American Physical Society [38, 37, 28]. These papers described a device called the "Hall Current ion accelerator" which bears much resemblance to the modern Hall thruster. Throughout the 1960's there was a flurry of research into the Hall thruster in the United States, until about 1968. In 1968, the former Soviet Union published their first experimental work on the Hall thruster [35]. Soon thereafter, the United States decided to focus on the development of the ion engine over the Hall thruster, as the ion engine has a higher theoretical specific impulse [9].

It was the former Soviet Union who launched the first Hall thruster in 1971 and

tested it on orbit throughout 1972 [27, 13]. They launched what is known as a stationary plasma thruster, one variant of the Hall thrusters developed by the former Soviet Union. The former Soviet Union, and then Russia, continued to develop, launch and use Hall thrusters on their satellites, for geostationary satellite final positioning and station keeping in the East/West direction by 1982 and the North/South direction by 1994. They launched over 140 satellites using Hall thrusters by 2001 [27].

It was this success of the former Soviet Union, and Russia after the Soviet Union fell, which propelled the United States back into the research and development of Hall thrusters in the early 1990's. NASA formed a program to evaluate the Russian technologies, and determined Hall thrusters afforded near optimal specific impulse and thrust-to-power ratios for Earth satellite applications [21]. From there, development continued and in 2006 the first Hall thruster launched by the United States, the Busek BHT-200 on TacSat-2 [1], hit orbit as part of a technology demonstration satellite. Development continues to improve the Hall thruster's performance and provide evidence inclusion of Hall thrusters will enable missions with significant mass and cost savings.

II. Background

2.1 Rocket Basics

The development, in Goebel and Katz, from force applied to thrust, Isp and efficiency, with corrections for non-ideal situations, is essential for the basic understanding of rockets and electric propulsion. The derivation here is applicable to spacecraft that are already in orbit, not launch vehicles. The comparison of chemical and electric propulsion systems is only relevant in space, as electric propulsion systems are incapable of space launch.

Spacecraft propulsion, whether chemical, nuclear or electrical, works by applying a force to the spacecraft by accelerating the propellant using Newton's equation

$$F = \frac{dp}{dt} \tag{1}$$

where p is the momentum and t is time. Assuming the rocket exhaust velocity is fixed the change in momentum is applied through a change in mass, ∂m, the force equation becomes

$$F = v_e \frac{\partial m}{\partial t} \tag{2}$$

The force on the rocket is also equal to the total mass of the rocket multiplied by the change in velocity of the rocket, or

$$F = M \frac{\partial v}{\partial t} \tag{3}$$

The total mass of the spacecraft is

$$M = m_{prop} + m_{dry} \tag{4}$$

where M is the total mass of the spacecraft, m_{prop} is the mass of the propellant, and m_{dry} is the dry mass of the spacecraft. The time rate of change of the mass is simply

$$\frac{\partial M}{\partial t} = \frac{\partial m_{prop}}{\partial t} \tag{5}$$

The two force equations are then set equal to each other and solved for the change in velocity

$$\Delta V = -v_e \frac{\partial M}{M} \tag{6}$$

Integrating the equation from initial to final velocity and from initial to final mass, it becomes

$$\Delta V = v_e ln \left(\frac{m_{dry}}{m_{dry} + m_{prop}} \right) \tag{7}$$

which becomes

$$\frac{m_{dry}}{m_{dry} + m_{prop}} = e^{\frac{-\Delta V}{v_e}} \tag{8}$$

when exponentiated. This is known as the ideal rocket equation [16, p. 15-17].

Specific impulse is defined as the ratio of thrust to the rate of propellant flow multiplied by the acceleration of gravity, which allows the units to be expressed as seconds and allowing comparison between various systems without having to convert units. Thus

$$I_{sp} = \frac{T}{\dot{m}_{prop}g} \tag{9}$$

where I_{sp} is the specific impulse, T is thrust, $\dot{m}_{prop}$ is the mass flow rate and g is the acceleration of gravity at the surface of the Earth, 9.807 m/s^2 [16, p. 25]. Using the definition of the thrust

$$T = \frac{\partial}{\partial t}(m_p v_e) = \dot{m}_{prop} v_e \tag{10}$$

to get

$$I_{sp} = \frac{v_e}{g} \tag{11}$$

which is substituted into Equation 8 to show

$$\frac{m_{dry}}{m_{dry} + m_{prop}} = e^{\frac{-\Delta V}{g I_{sp}}} \tag{12}$$

The dry mass of the spacecraft is given by

$$m_{dry} = m_{inert} + m_{pay} \tag{13}$$

where m_{inert} is the inert mass of the spacecraft and m_{pay} is the mass of the payload. This can be simplified by assuming that the entire spacecraft is payload, setting m_{inert} to zero, giving

$$m_f = \frac{m_{pay}}{m_{pay} + m_{prop}} = e^{\frac{-\Delta V}{g I_{sp}}} \tag{14}$$

where m_f is the payload mass fraction of the spacecraft. The mass fraction that is the payload for a given ∂V is calculated by inputing the I_{sp} into Equation 14. [18, p. 13] Thus the higher the I_{sp}, the greater the mass fraction of the spacecraft, which enables more payload capacity on the mission for a chemical rocket.

For electric propulsion systems another variable is added to the final mass of the spacecraft, m_{pwr}, the mass of the power system. Chemical rockets need little electrical power to work, and thus their power requirements are easily incorporated into the payloads power systems. Electrical propulsion systems often require different voltages and different current loads from the payload. These requirements necessitate additional power conditioning systems that increase the system mass. This complicates solving for payload mass fraction as it adds another mass term to Equation 13. In order to solve for the power system mass, power requirements for the thruster are

required. The jet power of an electric thruster is defined as

$$P_J = \frac{(I_{sp}g)^2 \dot{m}_{prop}}{2} \tag{15}$$

If the power source has an efficiency of η_t the power required from it is thus

$$P_s = \frac{P_J}{\eta_t} \tag{16}$$

If the power system has a specific power of α in W/kg then the mass of the power system is

$$m_{pwr} = \frac{P_s}{\alpha} \tag{17}$$

Equation 17 can be simplified by assuming a constant mass flow rate over the thrust duration, allowing

$$\dot{m}_{prop} = \frac{m_{prop}}{\tau} \tag{18}$$

where τ is the thrust duration. Substituting Equation 15 into Equation 16 and then substituting the result into Equation 17 and using Equation 18 results in

$$m_{pwr} = \frac{(I_{sp}g)^2 m_{prop}}{2\alpha\eta_t\tau} \tag{19}$$

then solving for the payload mass fraction to results in

$$\frac{m_{pay}}{m_{pay} + m_{prop}} = m_f = e^{\frac{-\Delta V}{I_{sp}g}} - \left(1 - e^{\frac{-\Delta V}{I_{sp}g}}\right) \frac{(I_{sp}g)^2}{2\alpha\eta_t\tau} \tag{20}$$

This shows there is an I_{sp} where the payload mass fraction is optimized depending on power system technology and mission requirements [18, p. 517-519].
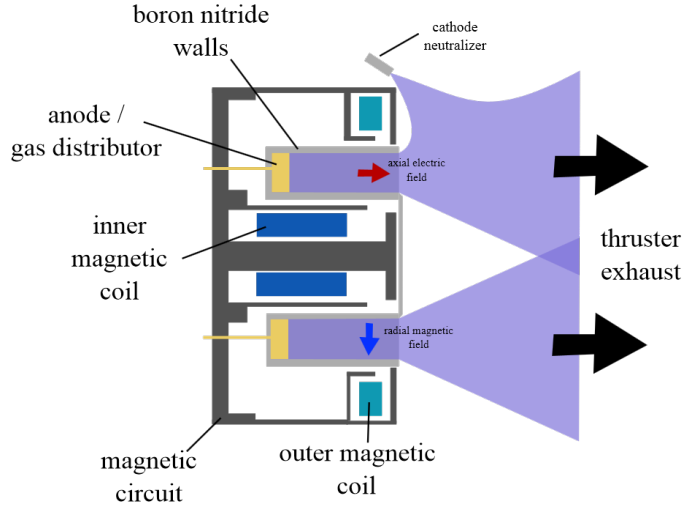
Figure 1. Schematic of an azimuthally symmetric Hall Effect Thruster showing the axial electric field and the radial magnetic field. [33].

2.2 Hall Thrusters

Hall Thrusters are a type of electric propulsion that work by trapping electrons in a crossed electric and magnetic field, creating the Hall current from which the thruster gets its name. The Hall current is used to ionize the propellant gas, usually Xenon due to its high mass and low ionization energy, which is then accelerated via the electric field to produce thrust. Figure 1 shows a schematic of a typical Hall thruster.

The crossed electric and magnetic fields create a force on the electrons preventing the electrons from quickly leaving the ionization zone of the thruster, moving through the zone in a Hall current at velocity

$$v_{elec} = \frac{\mathbf{E} \times \mathbf{B}}{B^2} \tag{21}$$

where $\mathbf{E}$ is the electric field vector, $\mathbf{B}$ is the magnetic field vector, and B is the magnetic field strength [16, p. 20]. This motion is sufficient for the electrons to

8

collisionally ionize the propellant gas as the propellant is fed into the chamber. The electrons eventually leave the zone due to collisional diffusion. The crossed electric and magnetic fields do produce a force on the ions, but the gyro radius of the ions is significantly larger than the acceleration zone, allowing its effects to be neglected. The gyro radius of a particle with velocity perpendicular to a magnetic field is

$$r_g = \frac{mv_{perp}}{qB} \tag{22}$$

where m is the particles mass, v_{perp} is the velocity perpendicular to the magnetic field, and q is the particle charge [19, p. 70]. For an electron in the magnetic field, assuming a Maxwellian velocity distribution for the electrons, Equation 22 is solved to yield the gyro-radius as

$$r_g = \frac{m_e}{eB}\sqrt{\frac{8kT_e}{\pi m}} = \frac{1}{B}\sqrt{\frac{8mT_{eV}}{\pi e}} \tag{23}$$

where T_e is the electron temperature in Kelvin, k is Boltzmann's constant (1.38×10^{-23} $m^2 kg/s^2 K$) , and T_{eV} is the electron temperature in electron volts [16, p. 331]. For a common measured temperature of 25 eV and 150 G field strength, Equation 23 calculates a gyro radius of 0.13 cm. The electron's gyro-radius is much less than the length of the ionization zone, typically a few centimeters.

Approximating the ion energy as the beam energy solves Equation 22 for the ions as a gyro radius of

$$r_i = \frac{1}{B}\sqrt{\frac{2M_iV_b}{e}} \tag{24}$$

where M_i is the mass of the ion, V_b is the beam voltage, and e is the charge of the electron, assuming singly charged ions. Common measured values of the radial magnetic field and energy are 150 G and 250 eV respectively. Using these values, Equation 24 evaluates to a gyro radius for Xenon ions of about 164 cm, which is

much greater than the ionization zone length. This allows the ions to almost ignore the effects of the magnetic field.

The key factors of performance for a propulsion device are the thrust, the specific impulse, and the efficiency. The thrust of an electric engine is almost entirely composed of the velocity contributions of the accelerated ions, as the ions velocity is much greater than any neutrals making it through the ionization zone. This allows Equation 10 to be approximated as

$$T \simeq \dot{m}_i v_i \tag{25}$$

The ion exhaust velocity, by energy conservation, is given by

$$v_i = \sqrt{\frac{2qV_b}{M_i}} \tag{26}$$

where V_b is the net beam voltage, q is the ion charge, and M is the ion mass [16, p. 22]. The beam current is related to the mass flow rate by

$$\dot{m}_i = \frac{I_b M_i}{e} \tag{27}$$

thus allowing the ion current and voltage to be used to get an expression for the thrust as

$$T = I_b \sqrt{\frac{2M_i}{q} V_b} \tag{28}$$

Equation 28 shows that increasing beam current gives a linear increase in thrust. It also shows increasing the voltage only increases the thrust by the square root of the voltage. This is an ideal case, where all atoms of the propellant are singly ionized and the beam is in line with the axis of thrust. A more realistic formula adds an

efficiency term, γ, which is

$$\gamma = \alpha F_t \tag{29}$$

where α is the correction for doubly ionized atoms and F_t is the correction for divergence angle of the thrust, giving a final equation for thrust as [16, p. 24]

$$T = \gamma I_b \sqrt{\frac{2M_i}{q}V_b} \tag{30}$$

Similarly, the specific impulse for an electric thruster needs to be modified since the thrust is primarily a factor of the ions, thus

$$I_{sp} = \frac{v_i \dot{m}_i}{g \dot{m}_{prop}} \tag{31}$$

This leads to the definition of the mass utilization efficiency

$$\eta_m = \frac{\dot{m}_i}{\dot{m}_{prop}} = \frac{I_b M_i}{e \dot{m}_{prop}} \tag{32}$$

which defines what fraction of the total mass flow is ionized, with the non-ionized portion being wasted mass as it does not contribute effectively to the thrust. This, along with Equation 30 gives

$$I_{sp} = \frac{\gamma \eta_m}{g} \sqrt{\frac{2eV_b}{M_i}} \tag{33}$$

for a corrected specific impulse equation. Again, it is shown in Equation 33 increasing the beam voltage only gives a benefit with the square root of the increase, while increasing the efficiency is a linear gain.

So far two efficiencies have been shown, the thrust efficiency, γ, and the mass

utilization efficiency, η_m. A third key efficiency term is the electrical efficiency

$$\eta_e = \frac{P_b}{P_T} = \frac{I_b V_b}{I_b V_b + P_0} \tag{34}$$

where P_0 is every other power input to the thruster. This includes the magnet power, cathode heater power, and keeper power on the Hall Thruster [16, p. 29].

The total efficiency of the thruster can be found by comparing the output power (jet power) with the total power input, giving

$$\eta_T = \frac{T^2}{2\dot{m}_{prop} P_{in}} \tag{35}$$

which becomes

$$\eta_T = \gamma^2 \eta_e \eta_m \tag{36}$$

giving a simple way of measuring the total efficiency of the thruster with measured quantities such as beam current, beam voltage, input power, and mass [16, p. 28-29].

2.3 Hall Thruster Plasma Oscillations

Breathing Mode.

The previous analysis made the assumption the Hall thruster essentially operates in a steady-state mode. This works to determine time averaged quantities and allow for mission planning. However, the plasma in the Hall thruster is not steady-state, rather it has many different oscillations present at any one time. These oscillations may affect the performance of the Hall thruster. Plasma oscillations in frequency bands ranging from 1 kHz to 60 MHz have been identified [10].

One of the most widely studied oscillation modes, and the focus of this effort, is in the 1-20 kHz band. This mode was identified in Russian literature in the 1970's as

a "loop" or "circuit" oscillation as it is sensitive to the circuitry of the system [10]. A numerical model by Boeuf and Garrigues explained the oscillation as a movement of the ionization zone [7]. This is caused by the large magnetic field near the exit of the thruster causing a large degree of ionization depleting the neutrals in the ionization zone. This causes the ionization zone to move upstream where the smaller magnetic field has a reduced rate of ionization. This reduction then starves the ionization zone of electrons, allowing the ionization zone to move downstream near the exit, where the cycle repeats itself. Boeuf and Garrigues were the source of the term "breathing" mode.

Another model, by Fife et al., describe the oscillation in a similar manner [22]. Their model showed the frequency of the oscillations can be determined by modeling the neutrals and ions in a "predator-prey" relationship, shown by

$$\frac{\partial n_i}{\partial t} = \xi T_e n_i n_n - n_i \frac{v_i}{L} \tag{37}$$

$$\frac{\partial n_n}{\partial t} = -\xi T_e n_i n_n + n_i \frac{v_i}{L} \tag{38}$$

where n_i is the ion population, n_n is the neutral population, v_i is the velocity of the ions, L is the length of the ionization zone, T_e is the electron temperature, and ξ is an ionization function. Assuming small perturbations, the first order approximation becomes

$$\frac{\partial^2 n_i'}{\partial t^2} + \xi T_e^2 n_{i,0} n_{n,0} n_i' = 0 \tag{39}$$

Equation 39 can be solved as an undamped harmonic oscillator, with a frequency of [22]

$$\omega = \frac{1}{L}\sqrt{v_i v_n} \tag{40}$$

Equation 40 reveals the frequency is inversely related to the ionization zone length

and increased by the ion velocity which is proportional to the beam voltage.

One of the predator-prey model's implicit assumptions is the neutrals are replenished throughout the ionization zone evenly, which is counter-intuitive. This led Barral and Ahedo to develop a convective wave model to account for the transport of neutrals through the zone [3]. They developed the characteristic frequency of the breathing mode to be [4]

$$\omega = \mathcal{O}\left(\sqrt{\frac{v_i v_n}{L^2}}\right) \tag{41}$$

which is of the same order as the "predator-prey" model.

They continue to develop the convective wave model and show, to first order, the plasma density behaves as a standing wave while the neutral transport behaves as a combination of a standing wave and convective wave. The convective wave, however, oscillates through the ionization zone, minimizing its overall contribution compared to the standing wave, giving rise to the frequency found in Equation 41. This works only when the mode is stable and linear as the frequency loses its dependence on the ion velocity. The non-linear modes are dependent on the transport velocity of neutrals only [5, 7].

Further research into the matching of the convective and the predator prey model resulted in an updated predator-prey model taking into account the transport of the neutrals. This is done by identifying two mostly overlapping regions, the ionization region and the avalanche region, and distinguishing between the population of neutrals in both regions versus the neutrals in the ionization region alone [6]. The ionization region is the region where ionization occurs, while the avalanche region is where the electrons released in the ionization region are accelerated and collisionally ionize additional neutrals. The corresponding model reads

$$\frac{dI}{dt} = \beta I(N - \bar{N}) \tag{42}$$

14

$$\frac{dN}{dt} = -\gamma IN + \frac{Q_0}{L}e^{-\gamma\int_{t-\tau}^{t} Idt} \tag{43}$$

where I is the discharge current, N is the time dependent volume averaged neutral density, $\bar{N}$ is the steady-state neutral density, γ is the effective ionization rate, Q_0/L is the stocking rate, τ is a time delay before the neutrals in the ionization only affect the avalanche region, and β is the integrated propensity for electron multiplication throughout the thruster. Using this model, the frequency for linear oscillation modes is determined by

$$Re(\omega) \simeq \sqrt{\beta\frac{Q_0}{L}e^{-\gamma\bar{I}\tau}} \tag{44}$$

which is the same as Equation 40 with the addition of a correction factor $\sqrt{e^{-\gamma\bar{I}\tau}}$ which is usually close to 1. Additionally, a damping rate is determined as

$$Im(\omega) \simeq \frac{\gamma\bar{I}}{2}cos(\tau Re(\omega)) \tag{45}$$

which shows the model is stable for small τ. The model becomes unstable at a value $\tau_c = \pi/(2Re(\omega))$, limiting the timescales the model can be applied to. The stability of the model is determined by the transit time of the neutrals from the ionization region into the avalanche region.

Additional, oscillatory modes are present in the Hall thruster discharge including a rotating spoke mode, first observed by Janes and Lowder [20], a gradient-induced azimuthal oscillation, and other higher-frequency oscillations [10]. These other oscillations are beyond the scope of this work. For additional information, Reference [10] provides a good resource for Hall thruster oscillations.

III. Setup and Methodology

The experiments were conducted at the Air Force Institute of Technology (AFIT) Space Propulsion Analysis and System Simulation (SPASS) laboratory. The SPASS laboratory consists of a large vacuum chamber, propellant tanks, feed through systems, and various diagnostic capabilities to study electric propulsion concepts and designs.

3.1 Vacuum Chamber

The SPASS vacuum chamber is a 2.5 m long by 2.0 m diameter stainless steel cylinder with a volume of approximately 6.5 cubic meters. The chamber has six window ports for visual and laser diagnostic entry, six gas feed lines, and six electrical connection ports. These ports are placed throughout the chamber to allow for control and monitoring of the thruster and experimental apparatus.

The vacuum chamber is pumped down with a Leybold Trivac D65B rotary vane mechanical pump to approximately 100 mTorr. Pressure is then reduced to approximately 10^{-5} Torr by a CVI Torrmaster TM250 cryopump and further reduced to operating conditions by four CVI Torrmaster TM500 cryopumps and a CRG012 internal cooled plate, utilizing compressed helium chilled to below 20 K to freeze particles to the cryoheads. Minimum operating pressure is approximately 10^{-7} Torr. Each pump has a rated pump speed of 4000 liters per second of Xenon, and the cooled plate has a pumping speed of 4900 liters per second, allowing for a total chamber pumping speed of 20,900 liters per second. The vacuum level achieved by the system was more than adequate for the 200 W thruster, and even with the 200 W thruster at full power the chamber pressure never reached above 5×10^{-5} Torr. Research by Randolph et al showed this pressure is sufficient for analysis of thruster performance [41]. Over

16

time, the cryoheads become coated with propellant and other particulates, causing a degradation of pumping speed. This necessitates the occasional cleaning of the cryo-heads, requiring pumping the chamber back to atmospheric pressure.

Internal to the chamber are two translation stages. The first is a three axis translation stage build by Aerotech providing a 60 cm range in the X-Y-Z plane with sub-millimeter accuracy, shown in Figure 2. Attached to the translation stage is a structure built of $80/20^{\mathrm{TM}}$ aluminum fittings to enable the mounting of the Hall thruster in an optimum position. This translation stage allows the Hall thruster to be aligned with an inserted probe after the chamber has been pumped down. The second translation stage consists of two linear and one rotational stepper motor with mounts for various probes, shown in Figure 3. The combination of the linear and rotational stages allows for sweeping in cylindrical coordinates allowing for measurements at a constant radius.

Propellant injection is controlled by four MKS model 180A flow controllers. Two of the controllers are set to provide 5-50 SCCM and the others 0-10 SCCM with an advertised accuracy of 0.01% of their maximum capacity. Management of the controllers is done with an MKS Type 247 four channel readout controller.

3.2   Hall Thruster

The nominal operating conditions for the Busek 200 W Hall thruster are shown in Table 1. The thruster is designed to run at 200 W, with a discharge voltage of 250 V and a discharge current of 800 mA. At the recommended optimum propellant flow rate the thruster is capable of achieving 12.8 mN of thrust at a specific impulse of 1390 seconds with a 45.5% efficiency [29, 34]. Power processing for the thruster was supplied by a Busek Corp Power Processing Unit (PPU) similar to flight hardware. The PPU was powered by a Sorenson DCS 55-55E power supply providing the nec-
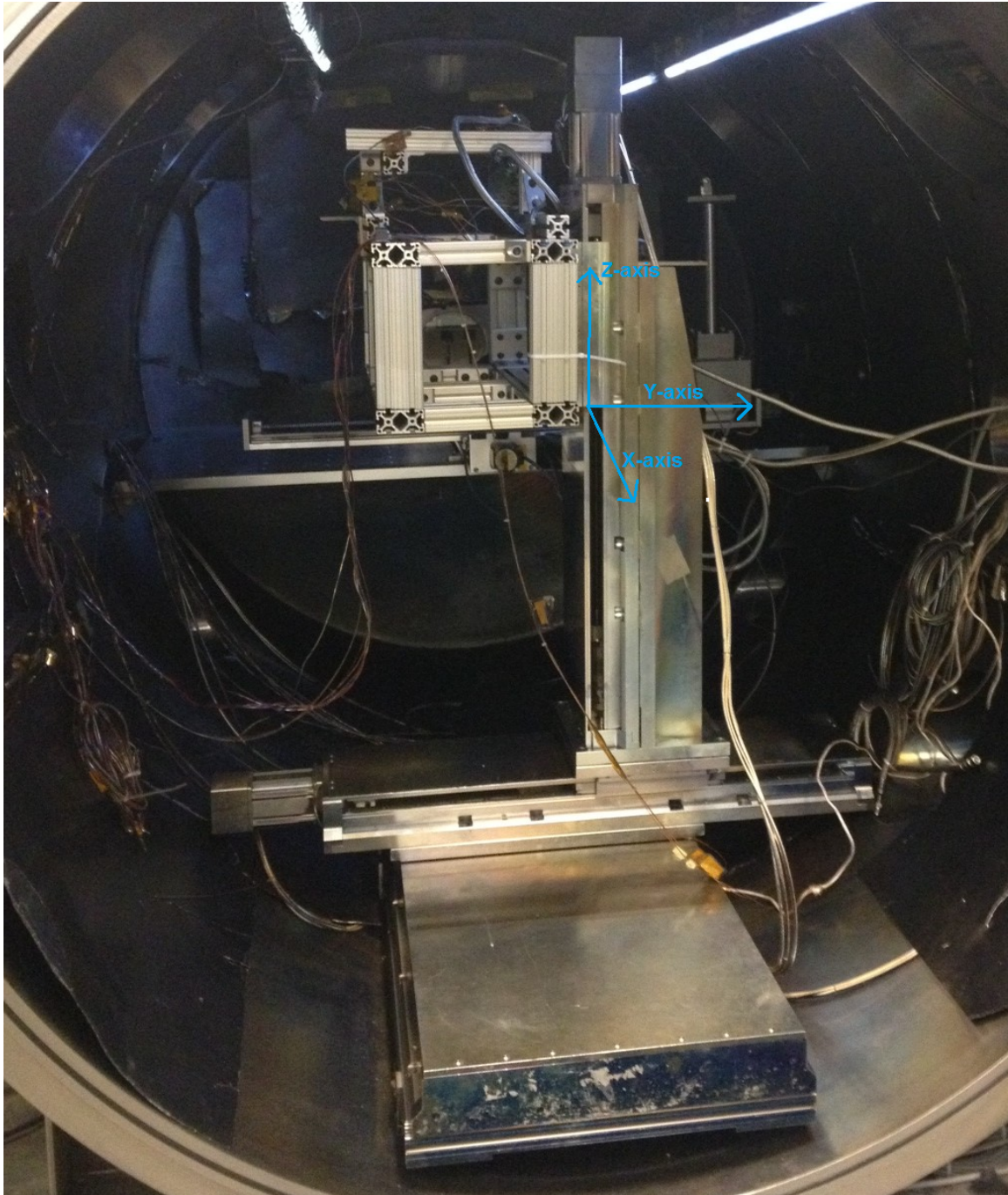
Figure 2. Translation stage for thruster positioning in the X-Y-Z plane. Sub-millimeter accuracy in the translation enables the thruster to be aligned to an inserted probe after the chamber is pumped down to vacuum.
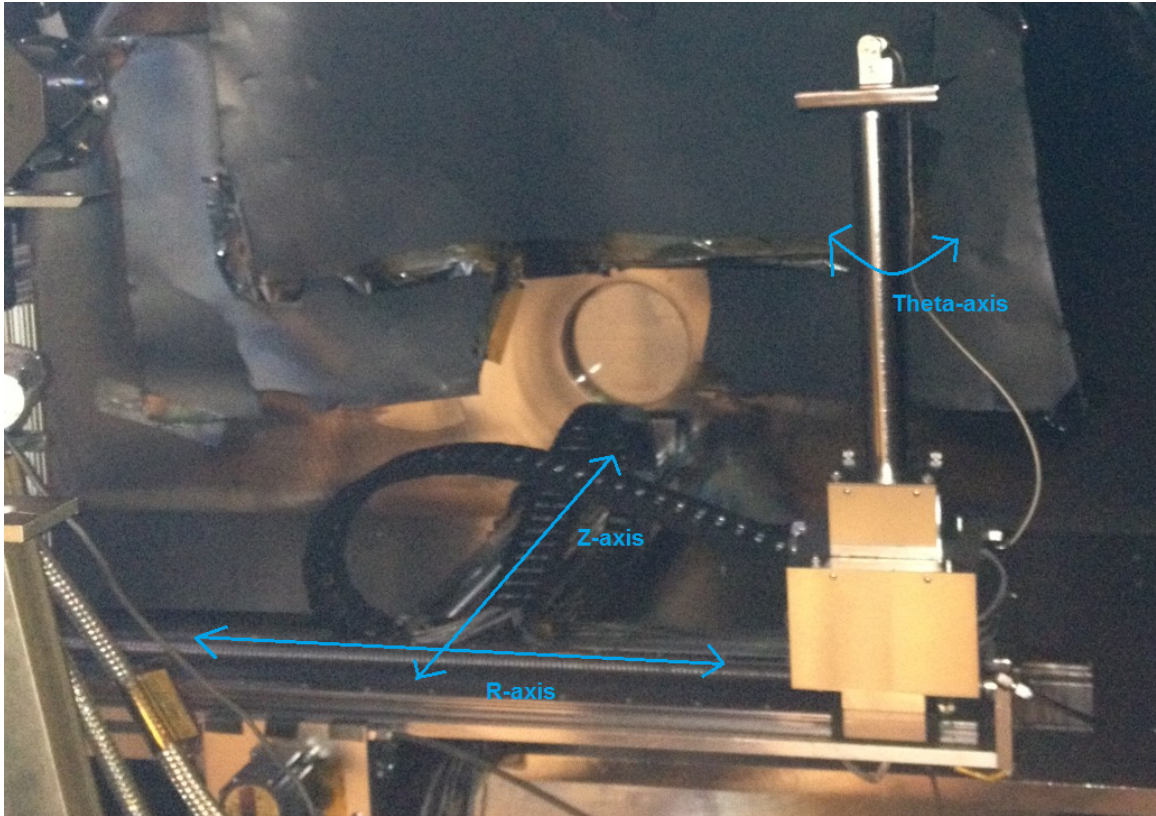
Figure 3. Translation stage for instrument sweeping with the Faraday probe mounted, showing axis of translation and rotation. The combination of R-Z-θ allows for scanning in cylindrical coordinates.

essary 28 V and up to 20 A to the PPU for the anode, cathode, magnet, and cathode heater. Normal operation is 28 V and approximately 9 A for a power draw of about 250 W total.

Table 1. Nominal Operating Conditions for Busek 200 W Hall Thruster

Anode Flow	840 μg/s (Xe)
Cathode Flow	98 μg/s (Xe)
Anode Potential	250 V
Keeper Current	0.5 A
Magnet Current	1.0 A

3.3 Faraday Probe

A shielded, or collimated, Faraday probe was used to measure the beam current density within the thruster plume. A shielded Faraday probe consists of a collector plate located behind a cap with a small aperture, shown in Figure 4. This enables the collector plate to only collect ions from the desired direction, reducing the effect of background charge exchange ions. Charge exchange ions are created by collisions between energetic ions and thermal neutrals which result in energetic neutrals and thermal ions. The ions accelerated from the Hall thruster are neutralized by electrons emitted from the cathode, making a quasi-neutral plasma. These electrons are rejected from the Faraday probe by biasing the probe cap to -20 V. If the electrons are not rejected, the total beam current measured would be near zero, as the electrons counteract the positive charge of the ions. The collector plate is biased 20 V from ground to repel any charge exchange ions managing to enter the aperture. The thermal ions created in the charge exchange process will not have enough kinetic energy to overcome the voltage barrier to interact with the collector plate. The ions impacting the collector plate induce a current through the circuit as electrons move to the surface of the collector plate to neutralize the ions. This movement of elec-
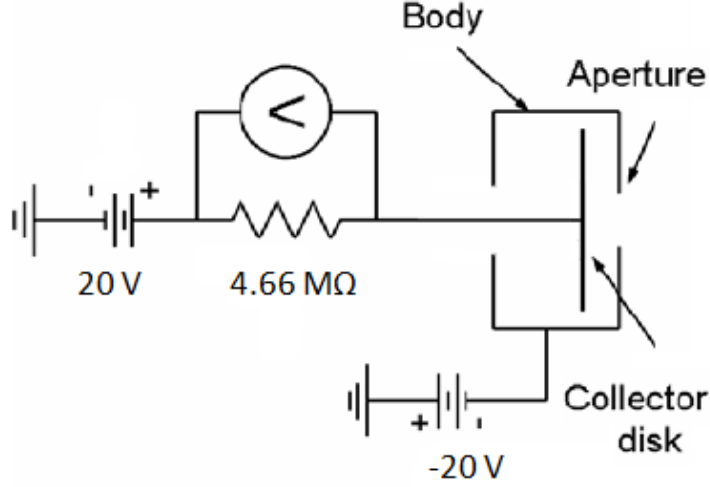
Figure 4. Electrical schematic of a shielded Faraday probe where the body is biased negative to repel plume electrons and the collection plate is biased positive to repel charge-exchange ions [14].

trons creates a measurable voltage drop across a resistor placed in the circuit. From the measured voltage the current density is calculated with the following relationship given by Farnell et al.

$$j_B = \frac{V * 1000}{R * A_{ap}} \tag{46}$$

where V is the voltage, R is the value of the resistor, A_{ap} is the area of the aperture and j_B is the current density in mA/cm^2 [14]. Additionally, the ions impacting on the collector plate can cause a secondary electron emission, where the impact ejects an electron from the plate, which results in a change in current. The biasing scheme described above creates a potential field forcing the secondary electrons emitted to return to the collector plate, thus negating the electrons contribution to the current.

Shielding the collector plate becomes important as the background pressure increases, especially when attempting to find the total extent of the beam current. Research by Manzella and Sankovic on an SPT-100 showed an increase in the beam

21
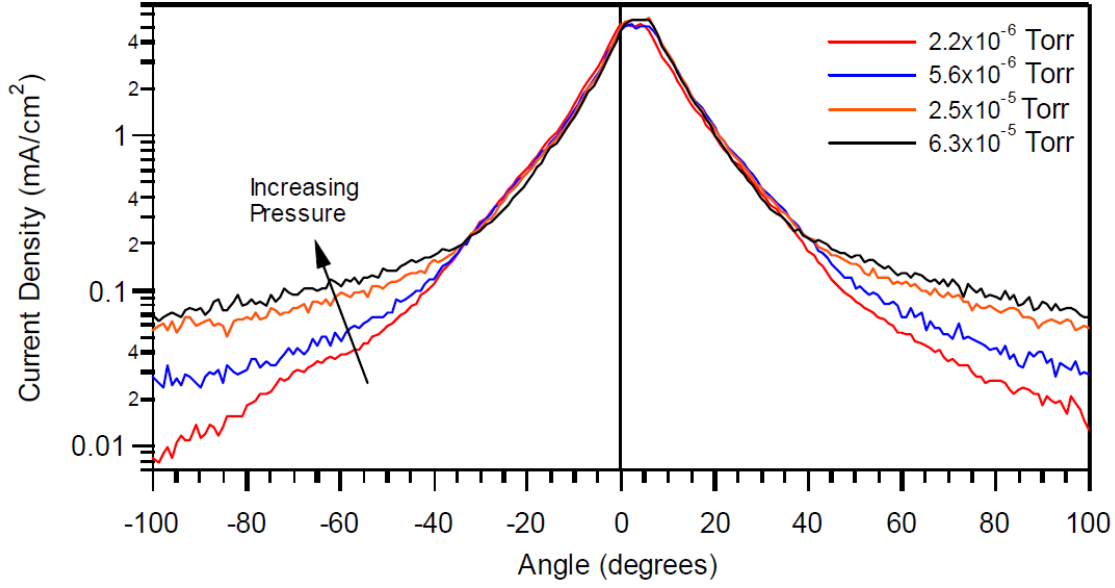
Figure 5. SPT-100 Current Density plotted at multiple background pressures. The increase in off-axis beam current is caused by an increase in plume charge exchange ions due to an increase in background pressure [32].

current density outside of 40° from centerline as chamber pressure increased, Figure 5. This increase in current density was caused by the increase in charge-exchange ions due to the higher chamber pressure.

One of the limitations of Equation 46 is the assumption the plasma originates from a point source and a correction factor needs to be inserted accounting for the cosine losses due to thruster geometry. These cosine losses cause a loss in the effective area of the aperture on the Faraday probe which, according to Equation 46, causes a decrease in measured beam current. Figure 6 gives a diagram of the system where R_{CL} is the distance from the centerline of the thruster to the center of the channels. The channel centerline is a more accurate location of where the ion production occurs. This distance is used to calculate the correction factor angles $\alpha_{L,R}$

$$\alpha_{L,R} = \pm \left(90 - \theta - tan^{-1} \left(\frac{cos(\theta) \mp \frac{R_{CL}}{R}}{sin(\theta)} \right) \right) \tag{47}$$

22

where R is the radial distance from the centerline of the thruster to the probe and θ is the angle from the thruster to the probe defined with 90 degrees being directly on the centerline. These angles are used to calculate a correction factor

$$\kappa_A = cos^2\left(\frac{\alpha_L + \alpha_R}{2}\right) \tag{48}$$

which is multiplied by the collection area of the probe to get a corrected collection area [8, p. 109-110].

Additionally, a distance correction factor must be determined, since the distance from the two channels to the Faraday probe are different from each other and the thruster center line. The correction factor averages the two distances to determine the radial distance from the thruster center line to determine the radial position of the probe. Utilizing the same diagram, Figure 6, the distances R_R and R_L are determined by

$$\frac{R_{L,R}}{R} = \sqrt{(sin(\theta))^2 + \left(cos(\theta) \mp \frac{R_{CL}}{R}\right)^2} \tag{49}$$

and the correction factor is then calculated as [8, p. 113]

$$\kappa_D = \left(\frac{1}{2}\left(\frac{R_L}{R} + \frac{R_R}{R}\right)\right)^2 \tag{50}$$

Together the two correction factors are used to calculate the total beam current using the following relationship

$$I_{Beam} = \pi R^2 \int_0^\pi j_B[\theta] \left(\frac{\kappa_D[\theta]}{\kappa_A[\theta]}\right) sin(\theta)d\theta \tag{51}$$

By calculating the correction factors given above, the systemic error of the Faraday measurements are reduced, providing a more accurate total beam current [8, p. 117].
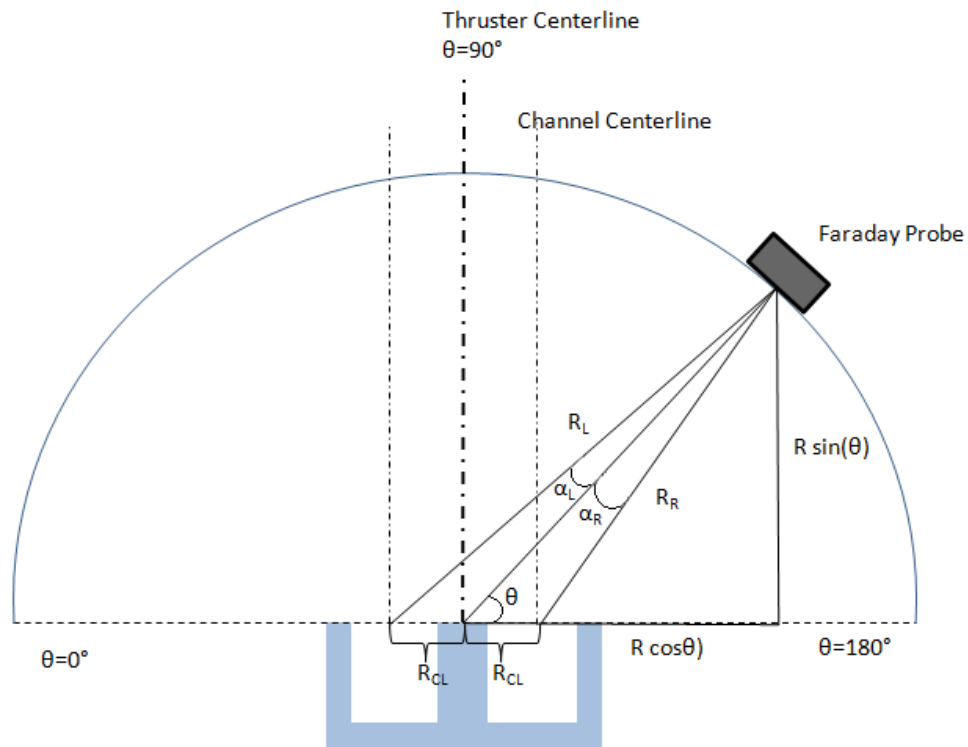
Figure 6. Diagram of Hall thruster and probe setup used to determine α_L and α_R to get the correction facter κ_A [8, p. 110]

IV. Results and Discussion

A total of eleven test runs were conducted with the thruster, six with xenon propellant and five with krypton propellant. The first three tests of each propellant were at recommended nominal conditions for the Busek 200 W thruster, seen in Table 1. The final three tests with xenon and final two with krypton were conducted with dampening on the root mean square (RMS) of the discharge current. The discharge RMS was monitored via a proprietary control card provided by Busek. The discharge RMS was thought to be proportional to the breathing mode oscillation amplitude and thus minimizing the discharge RMS would minimize the breathing mode amplitude. The control card actively managed the magnet current in order to minimize the discharge RMS.

4.1   Startup and Stabilization

The thruster startup procedure is initiated with heating the cathode for fifteen minutes by running a large current (6.5-7 A) through the heater circuit. The cathode keeper is then engaged at 650 V and 0.5 A to create a current ejecting electrons from the cathode into the thruster and plume. After the keeper has engaged, the discharge voltage is brought to 200 V, putting the thruster in ball mode. Ball mode in the Hall thruster is when the plasma formed in the thruster is unfocused by the magnetic field, resulting in a ball of plasma around the thruster channels. After engaging ball mode, the magnet current is brought to 1.0 A to focus the ball into a beam, putting the thruster in jet mode, its normal operating condition. The discharge voltage is then brought slowly from 200 V to 250 V and the thruster is allowed to stabilize. The xenon tests will be discussed first, as xenon is the predominant fuel of Hall thrusters.

Figure 7 shows the record of the temporal variation of the discharge current and
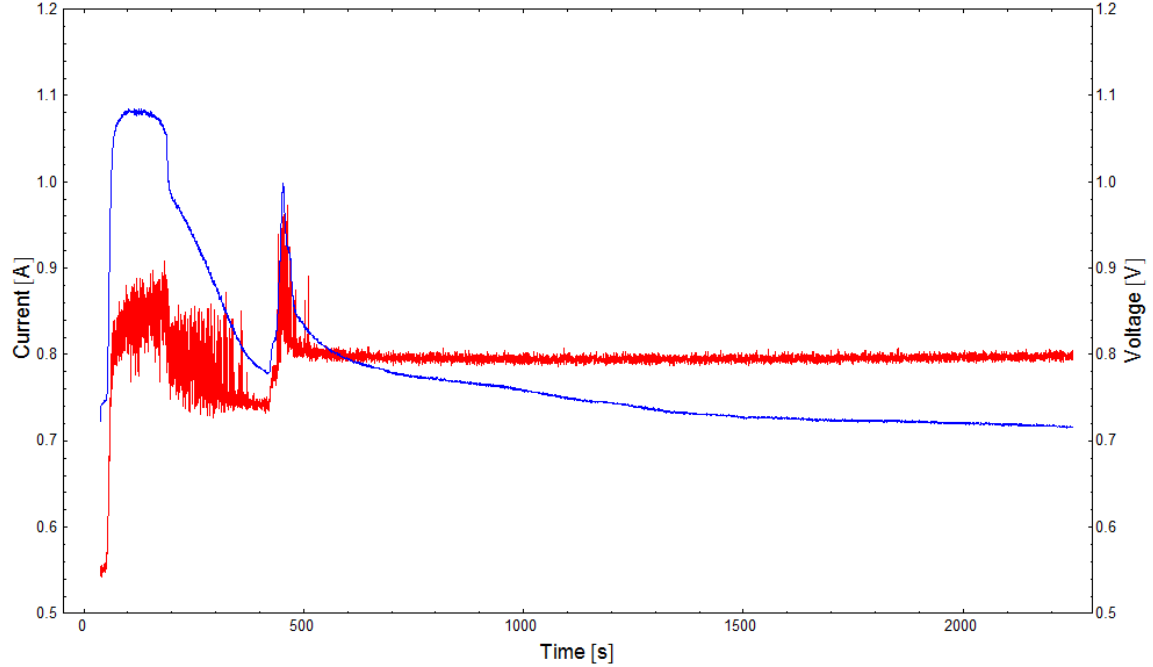
Figure 7. The discharge current (red) and discharge current RMS (blue) are plotted versus time from thruster startup with xenon propellant. Time 0 occurs when the discharge voltage is set to 250 V and magnet current to 1.0 A, the recommended nominal settings. The large oscillations in discharge current appear to indicate that the krypton was not fully purged from the propellant lines before startup. After the krypton is fully purged the current levels to the recommended optimal value of 0.8 A and the RMS appears to decrease asymptotically towards 0.7 V.

discharge RMS for the xenon test startup with the time beginning when the thruster operating conditions were set to the recommended nominal conditions shown in Table 1. The thruster control program records a data point at a rate of 4 Hz which enables some examination of time dependent effects but does not allow for direct measurement of oscillations. The large oscillations observed in the first 500 seconds are likely caused by a superposition of the krypton and xenon breathing mode oscillations, due to the propellant lines not being fully purged of krypton before running. After the krypton was purged, the discharge current stabilized to the recommended nominal value of 0.8 A, with the discharge RMS appearing to asymptotically approach a value of 0.7 V.

Figure 8 shows the record of the temporal variation of the discharge current and
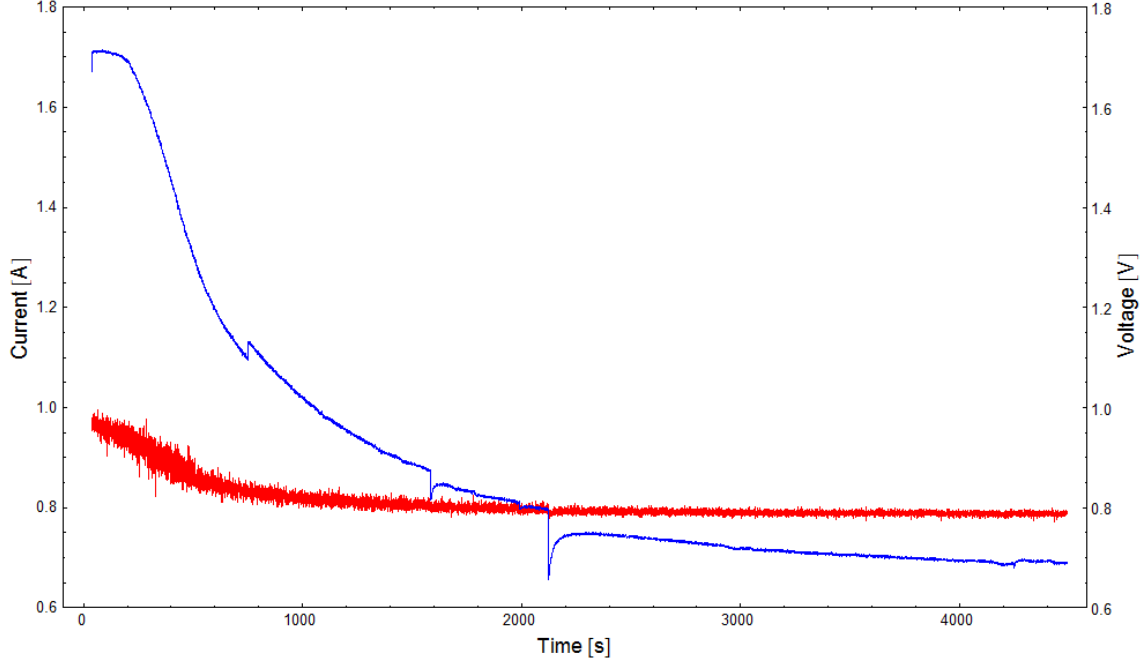
Figure 8. The discharge current (red) and discharge current RMS (blue) are plotted versus time from thruster startup with krypton propellant. Time 0 occurs when the discharge voltage is set to 250 V and magnet current to 1.0 A, the recommended nominal settings. Initial values are elevated for both, with both also trending to stable values. The discharge current decreases to the recommended optimal value of 0.8 amps, and the RMS appears to decrease asymptotically to 0.7 volts. The discontinuities in the RMS curve are likely caused by a sensor error.

discharge RMS for the krypton test startup. The krypton was held to the same conditions as the xenon with respect to the discharge current, discharge voltage, and the magnet current. The discharge RMS started at a large value of approximately 1.7 V, significantly larger than the xenon maximum of approximately 1.1 V. This is probably partially due to the thruster outgassing water molecules that disrupt the flow. The discontinuities in the exponential decrease of the discharge RMS are likely caused by a sensor error. The krypton discharge RMS did not approach the normal operating value of 0.7 V for almost 2500 seconds instead of xenon's 1500 seconds. This is likely due to the thruster being designed to operate with xenon as the propellant.

Both xenon and krypton propellants approached the same normal operating value of the discharge RMS because they were held to the same thruster conditions. The

magnet current, discharge voltage, and discharge current were held constant which forced the discharge RMS to the same value. This indicates the discharge RMS is either a function of those conditions or the thruster geometry, or most likely both. The predator-prey frequency model, Equation 40, indicates the discharge RMS is a function of the magnet field, and hence the magnetic current, and the discharge voltage. This shows that for the same magnet field strength and discharge voltage the frequency should be similar. The thruster was allowed to stabilize before taking the Faraday probe data of recommended optimal operation and engaging the discharge RMS control software.

4.2 Breathing Mode Stabilization in Xenon

Each of the first three xenon data sets were taken at distances ranging from 45 cm to 75 cm radially out from the thruster face. The Faraday probe was scanned as far in the angular direction as possible, however, it was limited by the configuration and geometry of the vacuum chamber and instrumentation setup shown in Figure 3. These limitations prevented the instrumentation from taking data through the full hemisphere. After three data sets were taken without the discharge RMS control activated, the discharge RMS control was activated. The discharge RMS control was allowed to run for ten minutes in the hope of stabilizing, which was not realized. After running for ten minutes, the Faraday probe was used to collect three more sets of current density data to assess the effect of the discharge RMS control.

The recorded discharge current, discharge RMS, and magnet current during the first Faraday probe scan are presented in Figure 9. The magnet current is being actively controlled in order to minimize the RMS. Initially, the magnet current stayed near the top end of the allowable range (maximum of 3 A) oscillating around 2.6 A resulting in a stable discharge current and discharge RMS. At approximately 6040

seconds a reduction in the magnet current was matched to a reduction in the discharge RMS causing the program to reduce the magnet current further in search of a new minimum. This rapid decrease in magnet current, and hence magnetic field strength, caused the thruster to drop out of jet mode. The loss of jet mode is indicated by the large increase in the discharge current, shown in red on Figure 13, without a corresponding increase in the beam current density detected by the Faraday probe, with Figure 13 showing the Faraday scan taken from approximately 6050 s to 6150 s. This increase is caused by the loss of the magnetic field strength, reducing the capability of the magnetic field to trap the electrons emitted by the cathode. The electrons not trapped create an almost DC signal, which drops the discharge RMS to nearly zero. The trapped electrons ionize neutral xenon particles, creating new trapped electrons. The electron number density slowly builds up until enough are trapped to create an avalanche in the ionization region, creating sufficient ions, produced in this process, to form a jet for a short period. This cycle of reduced ion flux followed by a surge is referred to as "chugging". The chugging effect causes the control software to see an increase in the RMS, so it alters the magnet current, maintaining the thruster in ball mode instead of allowing it to transition back to jet mode. This is seen in the oscillatory nature of the magnet current and discharge current.

Figure 10 shows an enlarged view of Figure 9 which is approximately matched to the data taken by the Faraday probe at 45 cm. The probe was started at 45 cm, taking two data points at every one degree between -36° and 36°. The two data sets, the Faraday probe and the thruster control software, were taken with two different computers, so the correlation between the two is an estimate, though care was taken during the xenon run to record start times of scans and attempt to match them. At each of the data points the probe waited 0.5 seconds, with an approximate translation speed of 1 second between each degree, which allowed for an estimate of the start

Figure 9. The discharge current in amps (blue), magnet current in amps (red), and the discharge current RMS in volts(brown) are plotted versus time from thruster startup in seconds with xenon propellant. The RMS dampening circuit was activated during this time, causing the wide variations in output. It is thought that the thruster was falling out of jet mode into ball mode when the magnet current would drop below 0.8 A.

Figure 10. The discharge current in amps (blue), the magnet current in amps (red), and the discharge current RMS in volts (brown) are plotted versus time from startup with xenon propellant. This figure is roughly correlated to the 45 cm Faraday probe data and indicates stability in the discharge current and RMS with large magnet current. The changes in the magnet current, from 2.2 A to 3 A, caused very minor fluctuations in the RMS and significant change was not seen until the magnet current dropped below about 0.8 A.

and end time of the Faraday scan at 45 cm to match to the thruster control software data. During the majority of the scan at 45 cm the magnet current was high and oscillating around 2.6 A. This increase in the magnet current caused an increase in the magnetic field strength. The increased magnet field strength caused the length of the ionization zone to increase. The large ionization zone enabled an increase in the propellant utilization efficiency, so more neutrals were ionized as they traversed the thruster channel. As a result, there was a corresponding increase in the measured beam current, as shown in the Faraday probe current density data, Figure 11. The small increase near 29° is most likely caused by the large change in the magnetic field strength sending more ions to the edges of the plume. The baseline data compares favorably with the data available [2, 36].

Figure 12 shows an enlarged view of Figure 10 approximately matched with the
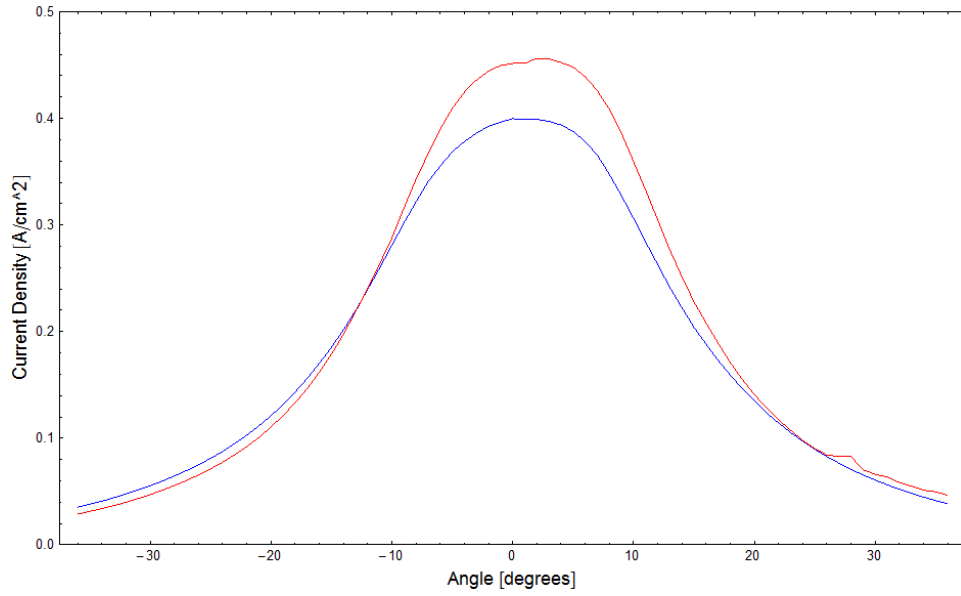
Figure 11. Faraday probe data collected by a sweep at 45 cm radial distance with the thruster using xenon propellant. Due to facility limitations, the sweep was only able to achieve +/- 36 degrees around center. The blue curve is the thruster operating at recommended optimal conditions (250 V discharge voltage, 0.8 A discharge current, 1.0 A magnet current, 0.962 mg/s mass flow rate) while the red curve is operated with the RMS dampening circuit active (250 V discharge voltage, 0.962 mg/s mass flow rate, magnet current variable with circuit activity).
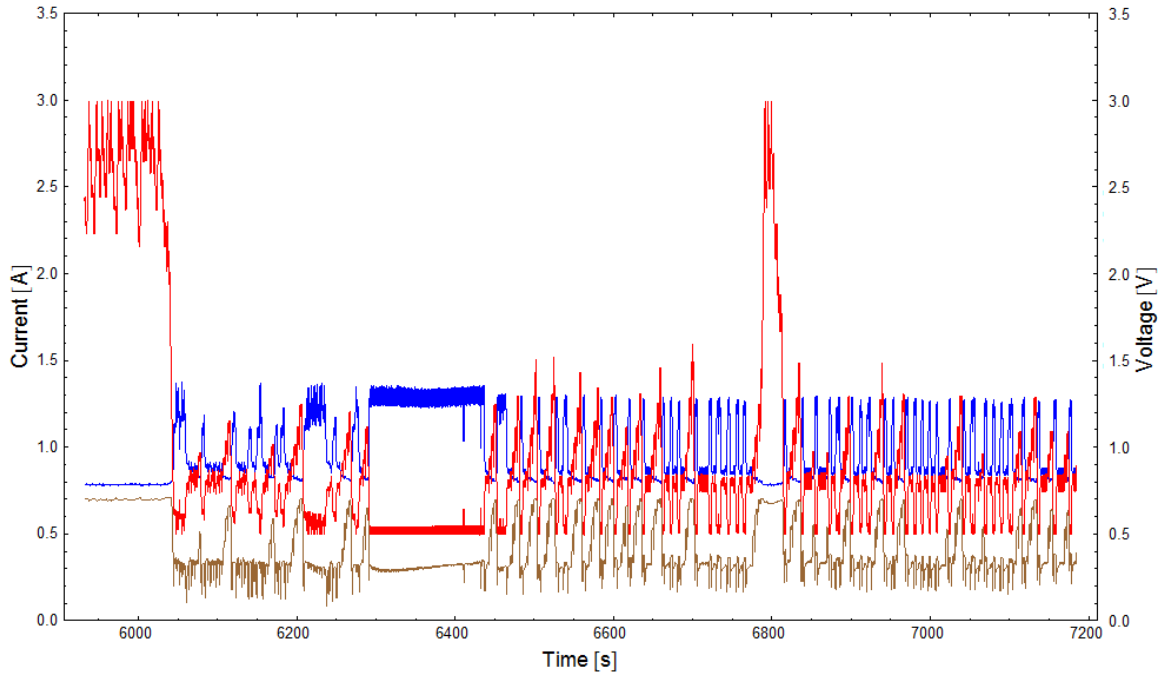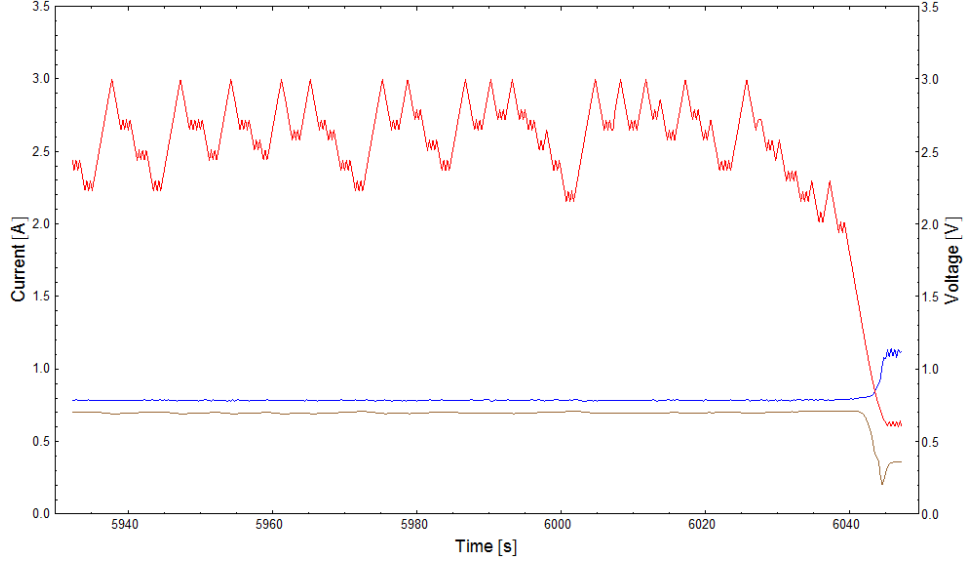
Figure 12. The discharge current in amps (blue), the magnet current in amps (red), and the discharge current RMS in volts (brown) are plotted versus time from startup with xenon propellant. This figure is roughly correlated to the 50 cm Faraday probe data. The magnet current is fluctuating severely, as the discharge RMS dampening circuit attempts to hold the RMS to a minimum, which forces the thruster out of jet mode and into ball mode.

data taken by the Faraday probe at 50 cm, immediately after the data taken at 45 cm. Throughout the majority of the data collection at 50 cm the thruster was oscillating between ball and jet mode as the discharge RMS control program attempted to minimize the discharge RMS by oscillating the magnet current around 0.7 A. This oscillation between ball and jet mode caused the beam current to become unsteady and lose around 20% of its beam current density, shown in Figure 13. The chugging caused by operating in ball mode forces a much lower utilization efficiency, reducing the number of neutrals ionized and thus the beam current. Further analysis of the beam current and utilization efficiency is provided in Section 4.4.

4.3 Breathing Mode Stabilization in Krypton

The krypton tests were accomplished before the xenon tests, allowing the xenon tests to benefit from the lessons learned over the krypton tests. The first two krypton

33

Figure 13. Faraday probe data collected by a sweep at 50 cm radial distance with the thruster using xenon propellant. This sweep was taken after the 45 cm data in Fig 11. During the sweep taken with the RMS circuit active (red) the thruster was alternating between jet and ball mode, creating an unsteady beam current density that is moderately reduced from the recommended optimal conditions (blue). The magnet current and discharge current for the unsteady curve are shown in Fig 14.

runs with the RMS control on were significantly more stable than the xenon test seen in Figure 9. The second run of krypton data experienced more oscillations similar to the xenon, seen in Figure 14, and is examined here. The majority of the data taken during the first two krypton RMS control runs had the magnet current oscillating around 2.8 A, resulting in a stable discharge current and a fairly stable discharge RMS. The discharge RMS varied more during this period, oscillating as much as 0.05 V around the 0.7 V equilibrium. This is due to krypton's higher ionization potential (14 eV versus xenon's 12.13 eV) causing a smaller ionization zone which fluctuated more strongly than xenon's. The ionization zone is smaller as there are less electrons with sufficient energy to ionize the krypton. The electrons with sufficient energy to ionize the krypton are more likely to be near the maximum of the magnetic field strength and less likely in the regions of lower magnetic field strength away from the face of the thruster.

While krypton's ionization zone is smaller than xenon's, the increased magnetic field strength during the run increases the size of the ionization zone above the recommended nominal conditions in the thruster. This larger ionization zone does not have as much of an effect on the utilization efficiency of the krypton, as shown in Figure 15. The overall increase is small, only 5% or so, which is within the systematic error of the Faraday probe. The data taken at 45 cm radial distance, Figure 15, is within the portion of the run where the magnet current oscillated around 2.8 A. It is estimated the latter half of Figure 16 occured during the drop out of jet mode around 7750 seconds, causing the decrease in beam current density. This decrease in beam current density is somewhat offset by the apparent reduction in the beam divergence angle, as measured by the full width at half maximum. More discussion of the beam divergence is in Section 4.4

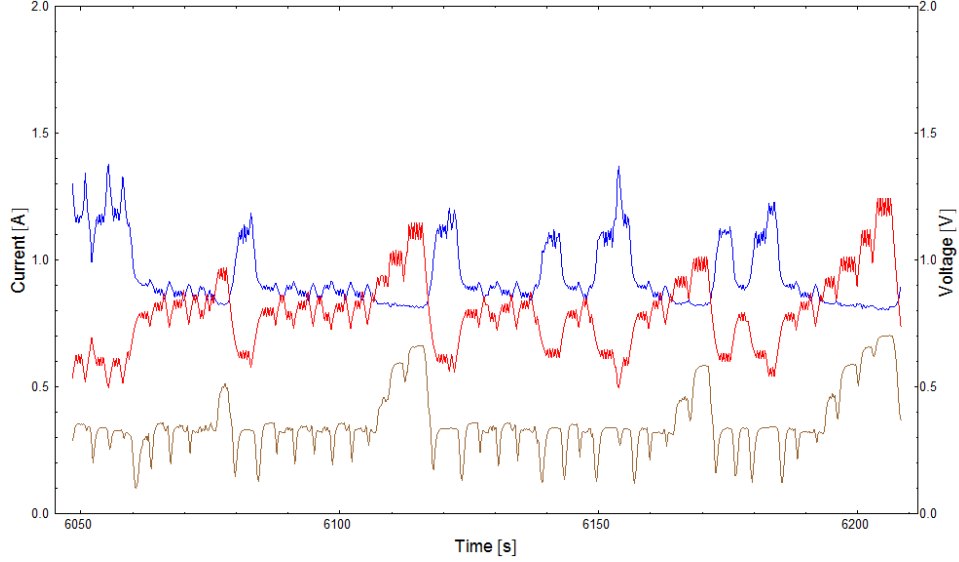Krypton dropped out of jet mode at approximately the same point as xenon, 0.8
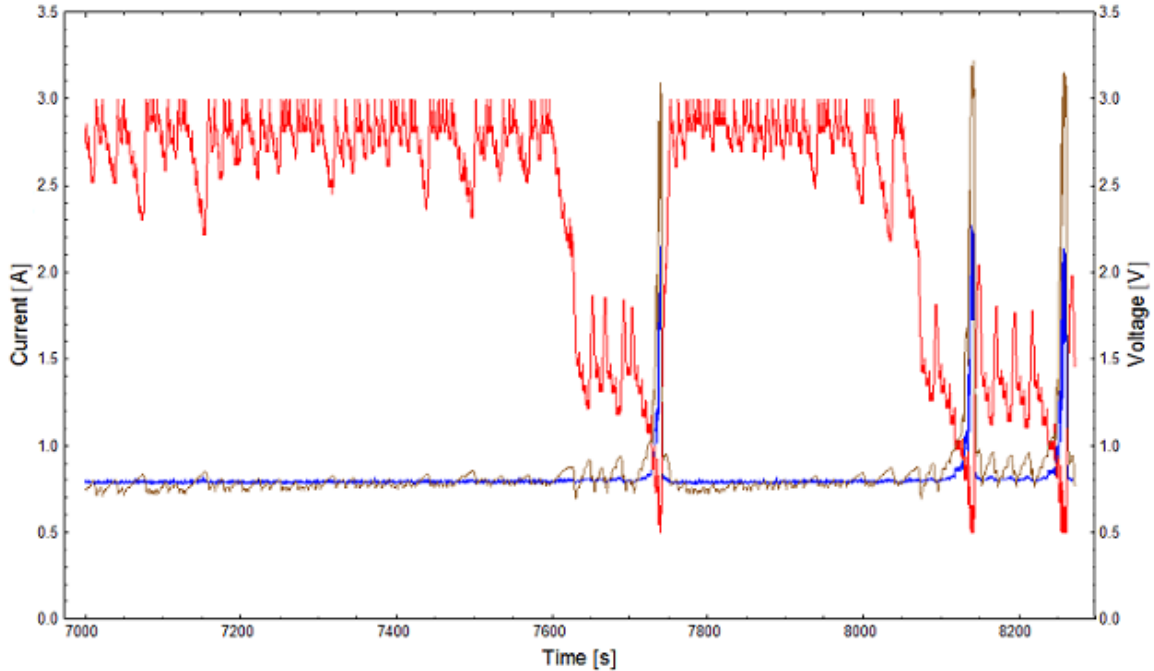
Figure 14. The discharge current in amps (blue), magnet current in amps (red), and the discharge current RMS in volts(brown) are plotted versus time from thruster startup in seconds with kryton propellant. The RMS dampening curcuit was activated during this run. As with the xenon, the thruster would fall out of jet mode if the magnet current dropped too low.

A magnet current, however the program almost immediately recovered and raised the magnet current, unlike xenon. This is due again to the difference in the ionization potential between the two gases, as when the thruster was in ball mode there were not enough electrons with a high enough energy to sustain ionization. This resulted in a large spike of discharge current where the full cathode output was absorbed, along with the electrons that were trapped before the magnetic field strength dropped. This spike in current caused a corresponding increase in the discharge RMS, which the control program rectified by increasing the magnet current above the jet mode threshold.
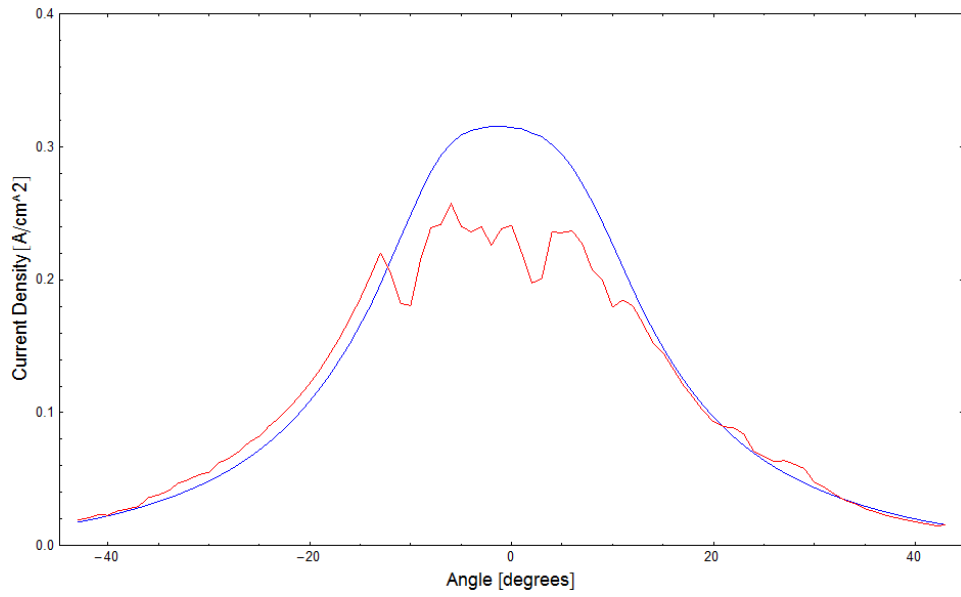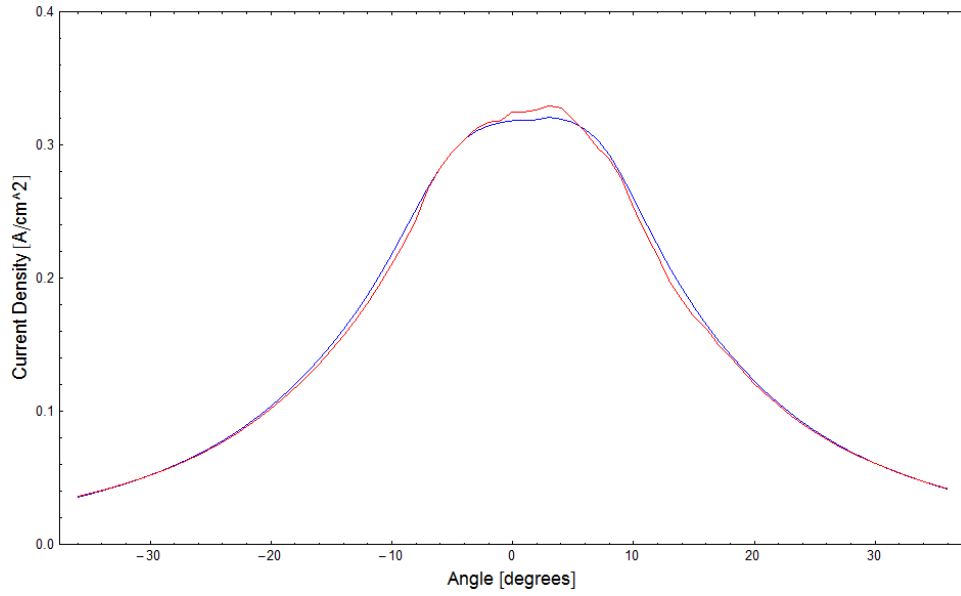
Figure 15. Faraday probe data collected by a sweep at 45 cm radial distance with the thruster using krypton propellant. The sweep taken with the RMS circuit active (red) shows a small increase in current density near the centerline compared to the sweep at recommended optimal conditions (blue).
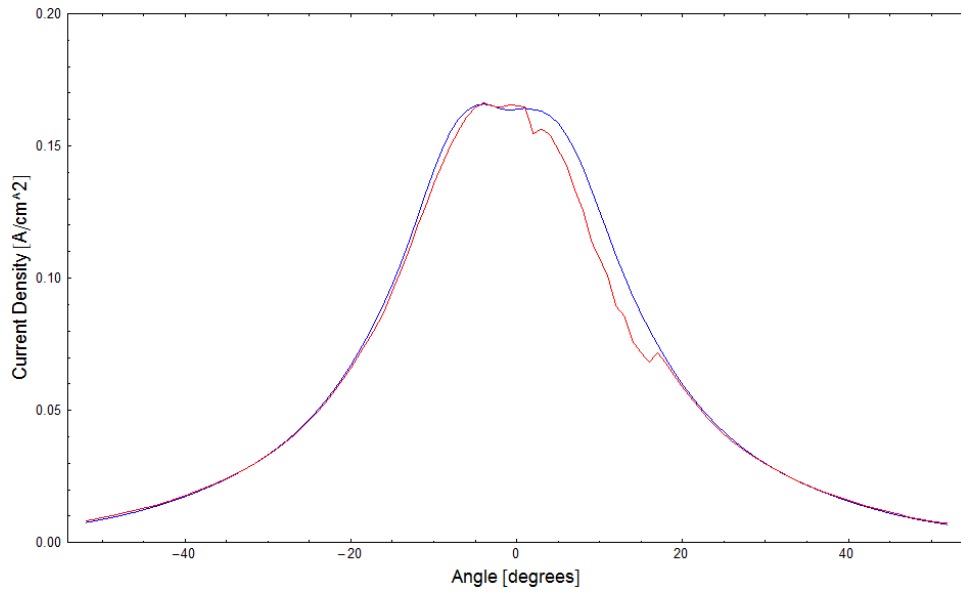
Figure 16. Faraday probe data collected by a sweep at 60 cm radial distance with the thruster using krypton propellant. The sweep taken with the RMS circuit active (red curve) shows some unsteadiness at this time, most likely caused by the loss of jet mode seen near 7750 seconds in Fig 14, which caused a decrease in the beam current.

4.4   Beam Current, Utilization Efficiency, and Divergence Angle

The Faraday probe data can be used to determine the total beam current by integrating the current density over the full hemisphere. The physical limitations of the diagnostic systems prevented the current density from being measured over the full hemisphere, thus requiring an approximation. The current density was assumed to decrease exponentially as $e^{-|\theta|}$ with the angle from centerline after ten degrees. This assumption allowed the use of Equation 51 to determine the total integrated beam current. The total integrated current from 45 to 75 cm radially from the thruster face is shown in Figure 17. The baseline data with no RMS control show a slight decrease over the distance due to ion-electron recombination and charge-exchange collisions with background and plume neutrals. The wide variation in the total current with RMS control activated is due to the large fluctuations with time that were seen in Figure 9.

The beam current efficiency is defined by Goebel and Katz as

$$\eta_b = \frac{I_b}{I_d} \tag{52}$$

where I_b is the integrated beam current and I_d is the measured discharge current [16]. Additionally, the propellant utilization efficiency is defined by Linnell [30], using the analysis of Hofer [17], as

$$\eta_p = \frac{\dot{m}_i}{\dot{m}_a} = \frac{M_i I_d}{\dot{m}_a e} \eta_b \Sigma \frac{\Omega_i}{Z_i} \tag{53}$$

where M_i is the mass of the ion, I_d is the discharge current, $\dot{m}_a$ is the anode mass flow rate, Ω_i is the current fraction of the ith charge species, and Z_i is the charge state of the ith species [30, 17]. These two equations are combined to allow the beam current to be used in place of the discharge current in Equation 53 by removing the η_b. Assuming a 10% doubly ionized rate, reasonable given data in [12], the propellant

Figure 17. The beam current integrated from the Faraday probe current density measurements are plotted versus radial distance for the thruster running with xenon propellant. When running at recommended nominal conditions (blue) the beam current decreases steadily with distance from approximately **0.79 A** to **0.73 A** due to charge exchange collisions and ion-electron recombination. The beam current measurements with the RMS circuit active (red) are almost all less than the recommended nominal conditions.

utilization efficiency for the average beam current at 45 cm is $105.9 \pm 2.2\%$ baseline and $106.9 \pm 5\%$ with RMS control active. An efficiency of greater than 100% is not realistic. The error is likely due to the thruster ingesting background neutrals, increasing the mass flow rate. To correct for the neutral ingestion, Equation 53 is solved for the mass flow rate assuming η_p is 1, $I_b = I_d$ and the propellant is singly ionized. This is then inserted into Equation 53 as the new mass flow rate. Using the corrected mass flow rate, an efficiency of $93.5 \pm 2\%$ is calculated for the baseline case. The efficiency with the RMS control active was calculated as $94.4 \pm 4\%$. The error in the calculation is due to the large fluctuations that occurred in the beam current. The error is large enough to obscure any gains or losses due to the RMS control. If only two of the three runs are included, the RMS control results in a calculated efficiency of $96.7 \pm 1.4\%$, as two of the three runs occurred during stable operation, similar to Figure 11, while the third occurred during unstable operation. This shows that, while the RMS control is stable and magnet current high, there is an increase in the propellant utilization efficiency. This increase comes at a cost, however.

The magnet current efficiency, η_{mag} is defined as

$$\eta_{mag} = \frac{P_d}{P_t} = \frac{1}{1 + \frac{P_{mag}}{P_d}} \tag{54}$$

where P_d is the discharge power, P_{mag} is the magnet power, and P_t is the total power [17]. At 45 cm the magnet current efficiency is $98.5 \pm 1\%$ for the baseline case and $89.6 \pm 1\%$ with RMS control active. The total efficiency of the two cases are the multiple of both efficiencies before, giving a total efficiency modification of $92.1 \pm 3\%$ baseline and $84.6 \pm 4.5\%$ with RMS control active.

The integrated beam current for the krypton data set is shown in Figure 18. The krypton data exhibited much less variation than the xenon data due to less time spent running in ball mode, as shown in Figure 14. The third run with RMS control was
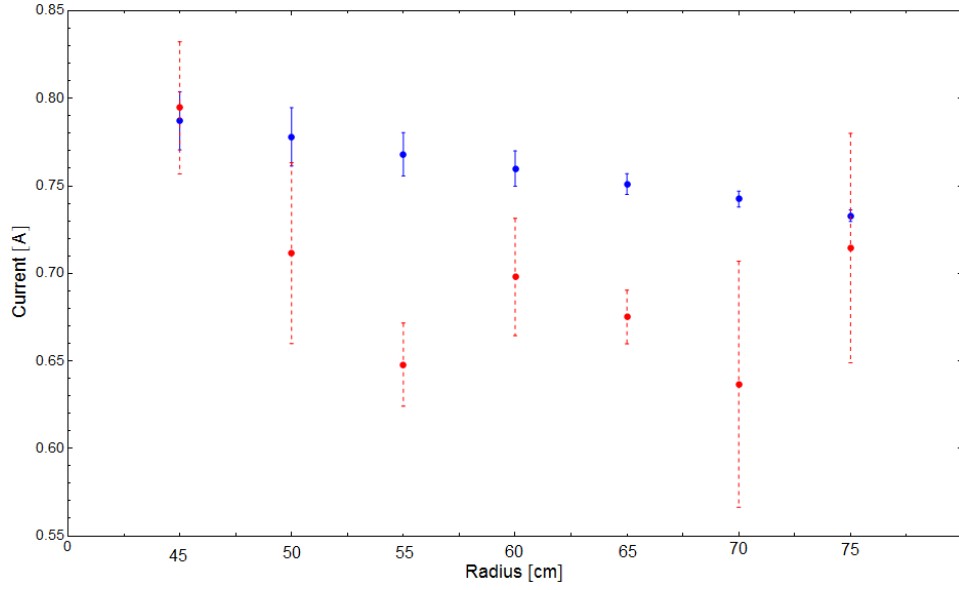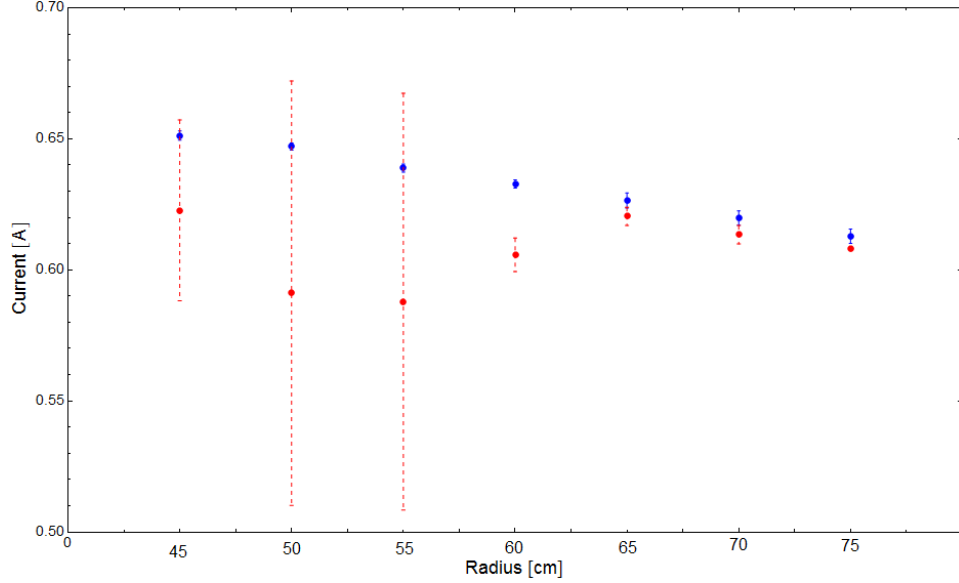
Figure 18. The beam current integrated from the Faraday probe current density measurements are plotted versus radial distance for the thruster running with krypton propellant. When running at recommended nominal conditions (blue) the beam current decreases steadily with distance similar to xenon. The beam current measurements with the RMS circuit active (red) show large error in the first measurements due to unstable operation conditions. The unstable run was terminated at the 55 cm line.

aborted due to large oscillatory behavior, as observed in the xenon data, before it was realized that the oscillations from ball to jet mode were important data. This ball to jet mode oscillation resulted in large error in the first three data points. The propellant utilization efficiency, calculated with Equation 53, for krypton is $73.2 \pm 1\%$ baseline and $70.0 \pm 4\%$ with the RMS control active. As with xenon, the error was significant enough to obscure any results. Additionally, two of the three runs were stable in the krypton run. Utilizing only the two stable runs, the propellant utilization efficiency is calculated as $72.2 \pm 1.5\%$. Unfortunately, the error is still too large to make a conclusion. The magnet current efficiency, calculated with Eq 54, was calculated as $98.1 \pm 1\%$ and $86.4 \pm 1\%$ respectively, resulting in an overall efficiency modification of $71.8 \pm 2\%$ and $60.5 \pm 4\%$, respectively.

Another factor in the efficiency of the thruster is the beam divergence angle. The

Figure 19. The beam divergence angle, as measured by the Full Width at Half Max of the current density from the Faraday probe data, is plotted versus the radial distance of the thruster running xenon propellant at recommended nominal (blue) and with the RMS dampening circuit active (red). The divergence angle increases with distance from the thruster due to collisions of ions with background or beam neutrals. The error of the data prevents making a determination on the effect of the RMS circuit.

calculated beam divergence angles with error for the xenon thruster is shown in Figure 19. The divergence angle was calculated by finding the full width at half maximum of the Faraday data, for example Figure 11. The error was calculated as sum of squares of the statistical error of the three runs and the measurement error of a half degree. The divergence angle of the baseline case increases with distance from the thruster due to collisional broadening, as the accelerated ions impact the background neutrals of the chamber. The highly unstable nature of the data taken with the RMS control active resulted in very large error, such that any determination of the effect of the RMS control on the divergence angle cannot be made.

The divergence angles with error for the krypton test series is shown in Figure 20. Unlike xenon, the thruster utilizing krypton propellant exhibited a decrease in the divergence angle, from $30.3 \pm 1°$ to $26.7 \pm 1°$. A simple correction factor for the
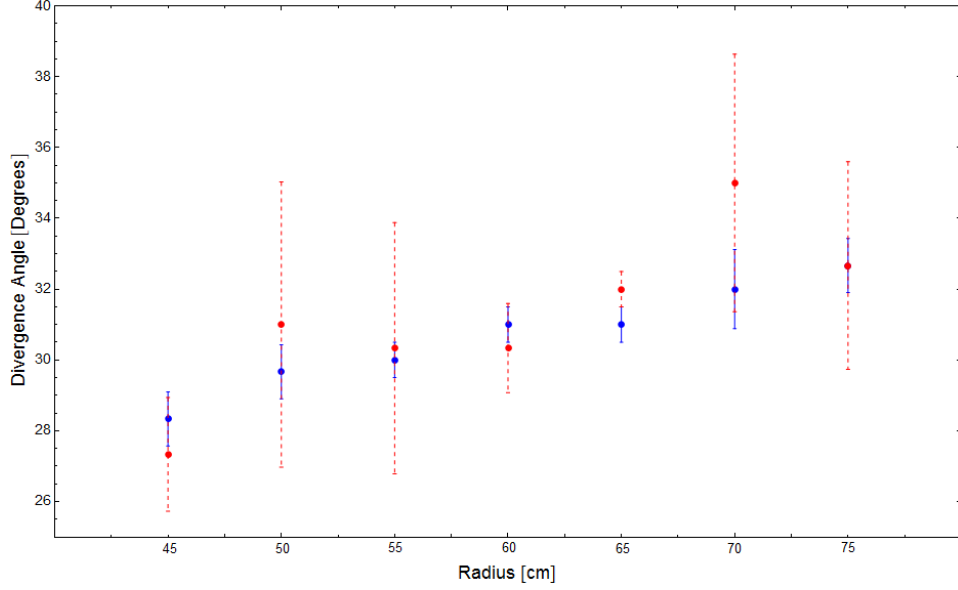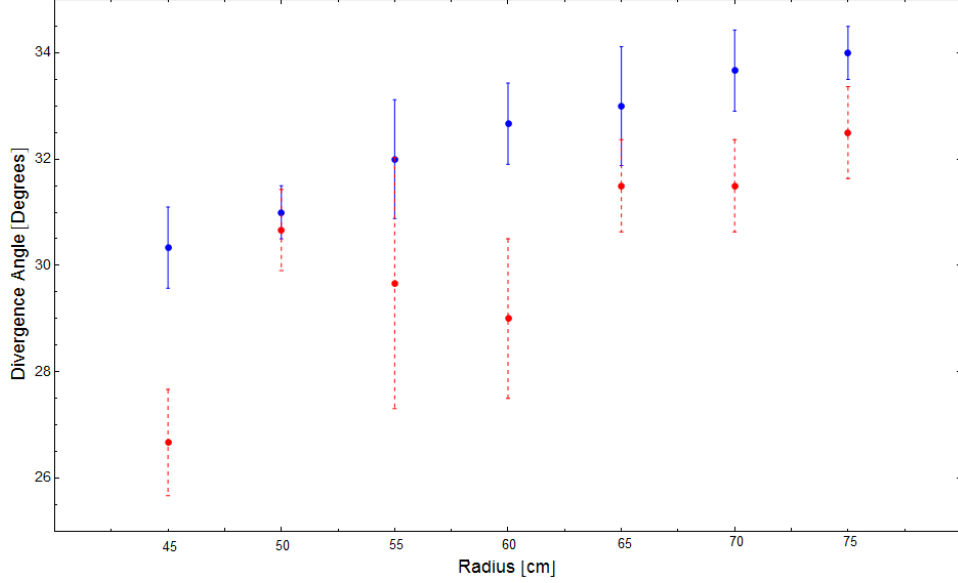
Figure 20. The beam divergence angle, as measured by the Full Width at Half Max of the current density from the Faraday probe data, is plotted versus radial distance of the thruster running krypton propellant at recommended nominal (blue) and with the RMS dampening circuit active (red). The data show that with the RMS circuit active the divergence angle is reduced for krypton.

divergence angle given by Goebel and Katz [16] is

$$F_t = cos(\theta) \tag{55}$$

where θ is the beam divergence half angle. At 45 cm, the krypton divergence correction factor is 0.965 baseline and 0.973 with RMS control active. Multiplying the correction factor into the total efficiency calculated earlier results in an overall efficiency modification of 69.9±1.5% and 58.9±4% respectively. If electrical power is not a concern, however, the magnet current efficiency can be left out of the calculation, resulting in an efficiency modification of $70.6 \pm 1\%$ and $68.1 \pm 4\%$, respectively.

The calculations given in this section were for the 45 cm data taken. The data taken at the other distances was not useful in the xenon case due to the large oscillations in discharge current. Trying to calculate a propellant utilization efficiency when

the thruster was running in the unstable mode would not be a useful data point. In the krypton case, the additional data is unenlightening, resulting in a similar conclusion in all cases.

The efficiencies calculated in this section can be used to make determinations of operating procedures and envelopes for the use of Hall thrusters in active spacecraft. Unfortunately, the large error in the data presented above prevents many conclusions from being drawn.

4.5 Analysis of Discharge RMS Effect on Breathing Mode Amplitude

An experiment to determine the effect of minimizing the discharge RMS on the breathing mode oscillation was conducted using an inductance probe. This experiment was accomplished after the Faraday experiments. The inductance probe was connected to the discharge current line and monitored through the use of an oscilloscope. The thruster was operated at recommended optimal values as shown in Table 1. The thruster was allowed to run for twenty minutes to stabilize before taking data. Figure 21 shows the discharge current versus time with an average oscillation amplitude of 0.85 A and an approximate frequency of 40 kHz. The discharge RMS was measured at 0.75 V during this scan. After taking the first scan, the discharge RMS control circuit was engaged and allowed to run for ten minutes.

A series of scans were then taken as the magnet current and discharge RMS varied. Figure 22 shows the discharge current versus time with the magnet current at 2.6 A. The average oscillation was reduced to 0.5 A while the discharge RMS was only reduced to 0.72 V. The approximate frequency was still 40 kHz. This shows even a minimal reduction in the discharge RMS had a large effect on the amplitude of the breathing mode oscillation. Figure 23 shows the discharge current versus time with the magnet current at 0.8 A. The magnet current had been at 0.5 A just before
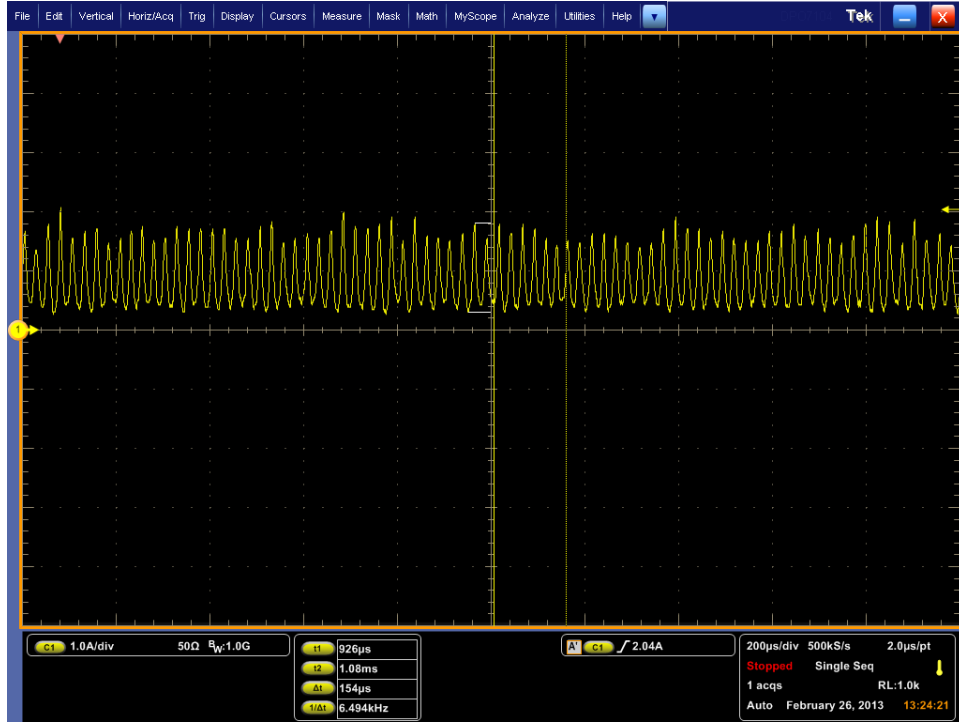
Figure 21. Oscilloscope trace of discharge current versus time for the recommended nominal operating conditions. Discharge RMS was measured at 0.75 V.

the scan. The discharge RMS was measured at 0.09 ± 0.02 V, the first time the error was significant. Evidence of chugging is distinct here, with the overlay of two oscillations. One oscillation has an amplitude of 0.45 A and a frequency of 10 kHz while the other has an oscillation of 0.15 A and an approximate frequency of 50 kHz. The chugging mode, as shown previously, is not the optimal mode for the thruster to run in, revealing that a large reduction in the discharge RMS or the magnet current drops the thruster into an inefficient mode.

45
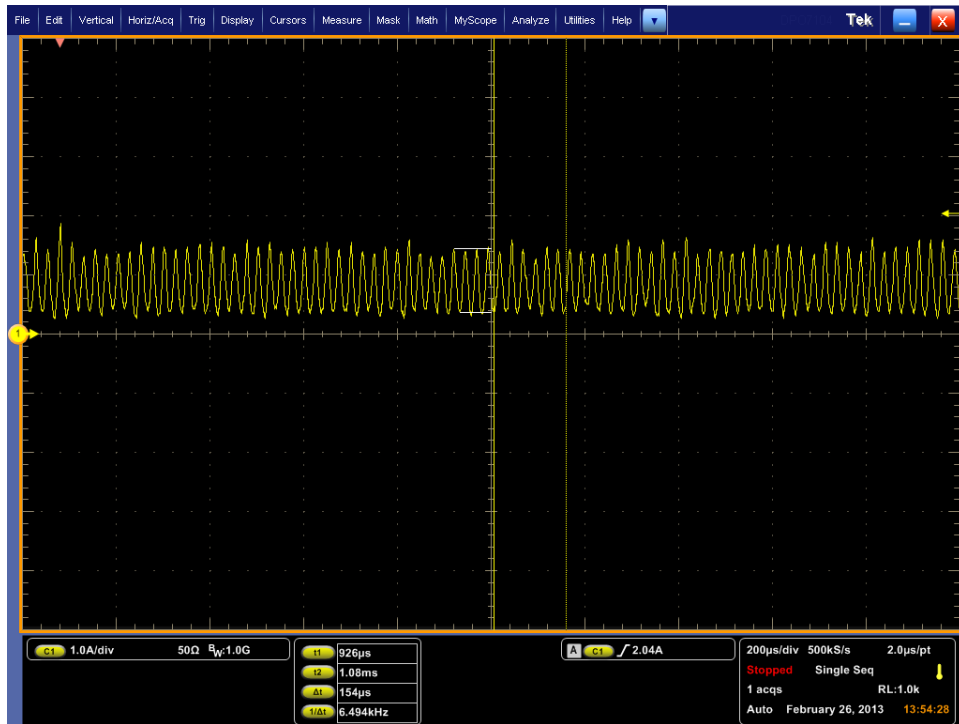
Figure 22. Oscilloscope trace of discharge current versus time with discharge RMS minimization active. Magnet current at time of capture was 2.6 A. Discharge RMS was measured at 0.72 V.

Figure 23. Oscilloscope trace of discharge current versus time with discharge RMS minimization active. Magnet current at time of capture was 0.8 A. Discharge RMS was measured at 0.09 V.

V. Conclusion

The overall effect of using active control of the magnetic field strength via the magnet current to actively reduce the breathing mode oscillation amplitude, measured by the discharge current RMS, reduced the total efficiency of the 200 W Hall thruster. The active control increased the propellant utilization efficiency in two cases, resulting in more neutrals getting ion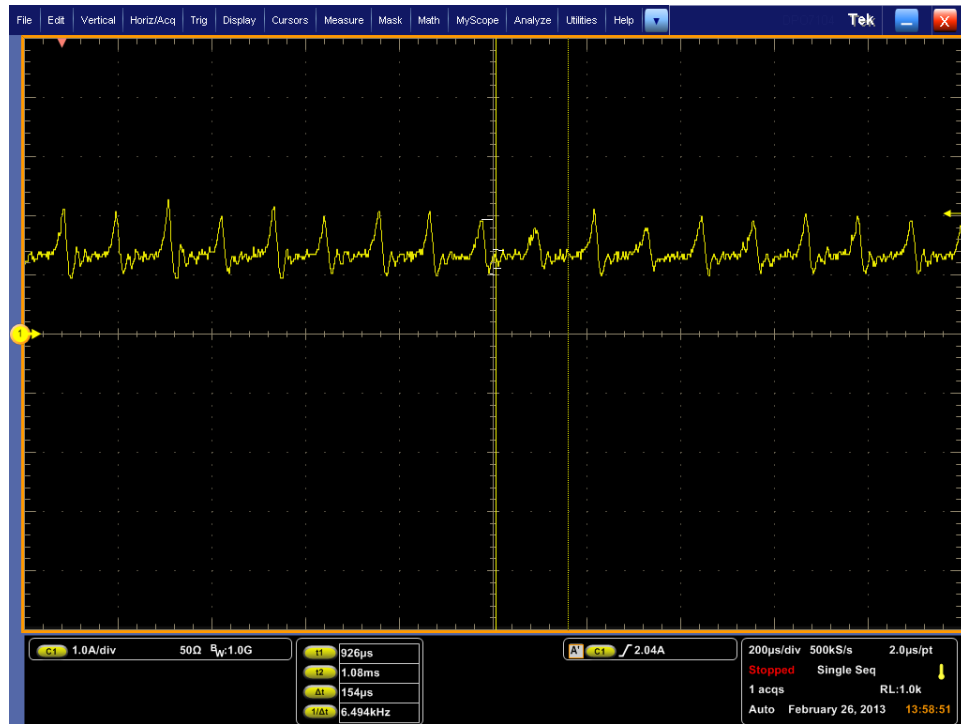ized, while reducing the magnet current efficiency. Together the two changes resulted in a decrease in the overall efficiency of approximately 5%. This increase in the propellant utilization efficiency can be beneficial in certain situations, even with the loss of electrical efficiency, if the satellite has the power available. High power communications satellites, and others whose payload requires as much or more power than the thruster, can take advantage of their excess power from the recommended optimal thruster operating conditions to gain the increase in the propellant utilization efficiency. This increase will allow the satellites to use less fuel for the same ΔV, enabling an increase in the satellite maneuvering lifetime. This benefit requires the satellite to have the extra power to overcome the loss in electrical efficiency triggered by the increase in the magnet current.

The beneficial effects of the RMS control on the propellant utilization efficiency were only seen in the thruster when running with xenon propellant. The data for the thruster running krypton propellant had sufficient error to obscure any beneficial or detrimental results. The krypton thruster did see a beneficial decrease in the divergence angle, which could result in a similar benefit to the increase in propellant utilization efficiency seen in the xenon thruster. Further research into the causes of the increase in propellant utilization efficiency for xenon and the decrease in divergence angle for krypton needs to be done with more diagnostics and more data points to reduce the error observed. This gives a starting point for the future work of this effort.

5.1 Future Work

The next steps for the research project presented here are to determine whether the benefits seen in the krypton and xenon thrusters are due to the active control of the discharge current RMS or simply from the large increase in the magnetic field strength through the large magnet current. To accomplish this, the thruster needs to be operated at a constant magnet current through the full range of the values seen in Figure 9, 0.5 A to 3 A, taking data with the Faraday probes to determine the effect on the propellant utilization efficiency and the divergence angle.

Additional experiments utilizing other diagnostic methods should be conducted to determine the full effect of the RMS control on the total efficiency. The study presented here focused on the divergence angle, magnet current efficiency, and the propellant utilization efficiency due to the available data and diagnostic systems. Other efficiencies need to be studied to get the full picture of the effect of the RMS control. Linnell and Hofer identify two other key efficiencies, the charge utilization efficiency and the acceleration efficiency, which might provide further insight.

The charge utilization efficiency can be determined using an ExB probe. ExB probes use an electric field and a magnetic field in a crossed field configuration to filter the ion beam by velocity. The current at a specific velocity setting, determined by $u = -E/B$, is then used to back out the ion species fractions of the thruster [36]. The ion species fractions are used to calculate the charge utilization efficiency with the best efficiency achieved with all of the ions being singly ionized.

The acceleration efficiency is determined by the ratio of the acceleration voltage to the discharge voltage and can be calculated by finding the average kinetic energy of the ions. An ExB probe can be used to determine this, using the velocity to find kinetic energy. A retarding potential analyzer can also be used to determine the kinetic energy of the beam, using grids to selectively filter the ions based on their

49

energy-to-charge ratios [30]. A better diagnostic tool to determine the average ion velocity and kinetic energy is laser induced flourescence (LIF), where a laser is used to excite the ions to an excited state that decays to a meta-stable state, resulting in photon emission. The photon emission is based upon the frequency of the laser and the ion velocity. The absorbtion spectrum of the ions will be shifted with respect to the laser due to the Doppler shift caused by the ion velocity. This shift can be measured by the emission of the excited ions allowing the velocity to be calculated. This technique has been used on both xenon [25, 24] and krypton [23, 26]. To utilize LIF in the SPAAS, however, a new laser for both xenon and krypton would need to be procured.

By utilizing the above diagnostic tools and test plans, a better understanding of the effect of active control of the discharge current RMS can be gained, and better options for mission planners and satellite system engineers can be determined.

Bibliography

1. `http://www.busek.com/flightprograms__ts2.htm`.

2. Yassir Azziz. Instrument development and plasma measurements on a 200-watt hall thruster plume. Master's thesis, Massachusetts Institute of Technology, September 2003.

3. Serge Barral and Eduardo Ahedo. Theoretical study of the breathing mode in hall thrusters. In *Proceedings of the 42nd AIAA Joint Propulsion Conference*, page 5172. American Institute of Aeronautics and Astronautics, 2006.

4. Serge Barral and Eduardo Ahedo. On the origin of low frequency oscillations in hall thrusters. *PLASMA*, page 439, 2008.

5. Serge Barral and Eduardo Ahedo. Low-frequency model of breathing oscillations in hall discharges. *Physical Review*, 79(046401):1, 2009.

6. Serge Barral and Zbigniew Peradzynski. A new breath for the breathing mode. In *Proceedings of the 31st International Electric Propulsion Conference*, University of Michigan, 2009.

7. J. P. Boeuf and L. Garrigues. Low frequeny oscillations in a stationary plasma thruster. *Journal of Applied Physics*, 84(7):3541, 1998.

8. Daniel Brown. *Investigation of Low Discharge Voltage Hall Thruster Characteristics and Evaluation of Loss Mechanisms*. PhD thesis, University of Michigan, 2009.

9. E. Y. Choueiri. Fundamental difference between the two Hall thruster varients. *Physics of Plasmas*, (8):5025, 2001.

10. E. Y. Choueiri. Plasma oscillations in Hall thrusters. *Physics of Plasmas*, 8(4):1411, 2001.

11. Edgar Choueiri. A critical history of electric propulsion: The first fifty years (1906-1956). In *Proceedings of the 40th AIAA/ASME/SAE/ASEE Joint Propulsion Conference and Exhibit*, Ft Lauderdale, Florida.

12. JM Ekholm and William Hargus Jr. E x b measurements of a 200w xenon hall thruster. *American Institute of Aeronautics and Astronautics*.

13. L.A. Artsimovich et al. Development of stationary plasma thruster (spt) and its test on board

14. Casey Farnell, Molly Schmidt, Robert Millot, Dustin Warner, Kyle Siler-Evans, and John Williams. Multi-axis plasma profiling system for characterization of plasma thruster plumes. In *Proceedings of the 42nd AIAA/ASME/SAE/ASEE Joint Propulsion Conference and Exhibit*, Sacramento, California, 2006.

15. Robert Goddard. Method and means for producing electricified jets of gas, December 1920.

16. Dan M. Goebel and Ira Katz. *Fundamentals of Electric Propulsion: Ion and Hall Thrusters*. JPL Space Science and Technology Series, 2008.

17. Richard Hofer. *Development and Characterization of High-Efficiency, High-Specific Impulse Xenon Hall Thrusters*. PhD thesis, The University of Michigan, 2004.

18. Ronald W. Humble, Gary N. Henry, and Wiley J. Larson. *Space Propulsion Analysis and Design*. Primis Custom Publishing, 1995.

19. Robert G. Jahn. *Physics of Electric Propulsion*. Dover Publications, Inc, 2006.

20. G.S. Janes and R.S. Lowder. Anomalous electron diffusion and ion accelertion in a low density plasma. *Physics of Fluids*, 9(6), 1966.

21. Robert Jankovsk, David Jacobson, Vincent Rawlin, Lee Mason, Maris Mantenieks, David Manzella, Richard Hofer, and Peter Peterson. In *Proceedings of the 37th AIAA, SAE, AIChE, and ASME Joint Propulsion Conference and Exhibit*, Salt Lake City, Utah, 2001.

22. Manuel Martinez-Sanchez John M. Fife and James Szabo. A numerical study of low-frequency discharge oscillations in hall thrusters. *American Institute of Aeronautics and Astronautics*, 1997.

23. William Hargus Jr. A preliminary study of krypton laser induced flourescence. In *Proceedings of the 46th AIAA/ASME/SAE/ASEE Joint Propulsion Conference*, 2010.

24. William Hargus Jr and M.A. Cappelli. Laser induced fluorescence measurements on a laboratory hall thruster. In *Proceedings of the 34th AIAA/ASME/SAE/ASEE Joint Propulsion Conference*, 1998.

25. William Hargus Jr and Michael Nakles. Ion velocity measurments within the acceleration channel of a low-power hall thruster. *IEEE Transactions on Plasma Science*, 36(5), 2008.

26. William Hargus Jr, Michael Nakles, and Gregory Azarnia. Demonstration of laser induced flourescence on a krypton hall effect thruster. In *Proceedings of the 32nd International Electric Propulsion Conference*, 2011.

27. Vladimir Kim, Garri Popov, Boris Arkhipov, Vyacheslav Murashko, Oleg Gorshkov, Anatoly Koroteyev, Valery Garkusha, Alexander Semenkin, and Sergei Tverdokhlebov. Electric propulsion activities in russia. *Electric Rocket Propulsion Society*.

28. E. C. Lary, R. G. Meyerand, and F. Salz. *Bulletin of the American Physical Society*, 7(441), 1962.

29. Daniel Lee. Velocity plume profiles for hall thrusters using laser diagnostics. Master's thesis, Air Force Institute of Technology, June 2010.

30. Jesse Linnell and Alec Gallimore. Efficiency analysis of a hall thruster operating with krypton and xenon. *Journal of Propulsion and Power*, 22(6), November-December 2006.

31. David Liu. *Two-Dimensional Time-Dependant Plasma Structures of a Hall Effect Thruster*. PhD thesis, Air Force Institute of Technology, September 2011.

32. David Manzella and John Sankovic. Hall thruster ion beam characterization. In *Proceedings of the 31st Joint Propulsion Conference and Exhibit*, San Diego, CA, 1995.

33. Finlay McWalter. `http://en.wikipedia.org/wiki/File:Wfm_hall_thruster.svg`.

34. Bryan Morgan. Building of a laser diagnostic tool to measure the ion velocity in a low power hall thruster. Master's thesis, Air Force Institute of Technology, March 2009.

35. A. I. Morozov, A. Y Kislow, and I P Zubkov. *JETP Letters*, 7(211), 1968.

36. Michael Nakles, Lubos Brieda, Garret Reed, William Hargus Jr, and Randy Spicer. Experimental and numerical examination of the BHT-200 hall thruster plume. In *Proceedings of the 43rd AIAA/ASME/SAE/ASEE Joint Propulsion Conference and Exhibit*, 2007.

37. F. Salz, R. G. Meyerand, and E. C. Lary. *Bulletin of the American Physical Society*, 7(441), 1962.

38. G. Seikel and E. Reshotko. *Bulletin of the American Physical Society*, 7(414), 1962.

39. L. R. Shepherd and A. V. Cleaver. The atomic rocket - 4. *Journal of the British Interplanetary Society*, (8):59.

40. Lyman Spitzer. Interplanetary travel between satellite orbits. *Journal of the American Rocket Society*, (22):92.

41. H. Kaufman K. Kozubsky V. Zhurin T. Randolph, V. Kim and M. Day. Facility effects on stationary plasma thruster testing. In *Proceedings of the 23rd International Electric Propulsion Conference*, Seattle, WA, 1993.

42. M. K. Tikhonravov, editor. *Works on Rocket Technology by E. K. Tsiolkovsky*. Publishing House of the Defense Ministry, Moscow, 1947.

REPORT DOCUMENTATION PAGE

Form Approved
OMB No. 0704–0188

1. REPORT DATE *(DD–MM–YYYY)*	2. REPORT TYPE	3. DATES COVERED *(From — To)*
21–03–2013	Master's Thesis	Sept 2011 — Mar 2013

4. TITLE AND SUBTITLE

EXPERIMENTAL ANALYSIS OF DAMPENED BREATHING MODE OSCILLATION ON HALL EFFECT THRUSTER PERFORMANCE

5a. CONTRACT NUMBER

5b. GRANT NUMBER

5c. PROGRAM ELEMENT NUMBER

6. AUTHOR(S)

Vineski, Christopher D., Captain

5d. PROJECT NUMBER

5e. TASK NUMBER

5f. WORK UNIT NUMBER

7. PERFORMING ORGANIZATION NAME(S) AND ADDRESS(ES)

Air Force Institute of Technology
Graduate School of Engineering and Management (AFIT/EN)
2950 Hobson Way
WPAFB OH 45433-7765

8. PERFORMING ORGANIZATION REPORT NUMBER

AFIT-ENY-13-M-39

9. SPONSORING / MONITORING AGENCY NAME(S) AND ADDRESS(ES)

Mr. Michael Huggins
AFRL/RQR
5 Pollux Dr
Edwards AFB Ca 93524
DSN 525-5230, COMM 661-275-5230

10. SPONSOR/MONITOR'S ACRONYM(S)

AFRL/RQR

11. SPONSOR/MONITOR'S REPORT NUMBER(S)

12. DISTRIBUTION / AVAILABILITY STATEMENT

DISTRIBUTION STATEMENT A:
APPROVED FOR PUBLIC RELEASE; DISTRIBUTION UNLIMITED.

13. SUPPLEMENTARY NOTES

14. ABSTRACT   Experiments were performed at AFIT to determine the effect of active control of the magnetic field strength to reduce the breathing mode oscillation on the efficiency of a 200W Hall thruster. The breathing mode oscillation amplitude was measured by the root mean square (RMS) variation in the AC portion of the discharge current. Experiments were run using krypton and xenon propellant. Using the xenon propellant control of the RMS improved the propellant utilization efficiency by approximately 2% in two cases, while reducing the magnet current efficiency by about 10%. Control of the RMS's effect on the divergence angle of the plume was unable to be determined due to error. The overall effect was to decrease the total efficiency by about 5%. Using krypton, the effect on the propellant utilization was unable to be determined due to error. Control of the RMS decreased the magnet current efficiency by about 11%. The divergence angle was reduced by about 3°, resulting in an overall decrease in total efficiency of about 6%. Overall, utilizing control of the RMS can be useful in satellites whose payload requires more power than the thruster, as they would be able to make use of the increase in propellant utilization without exceeding power capabilities.

15. SUBJECT TERMS

Hall Thruster, electric propulsion, oscillatory modes, efficiency

16. SECURITY CLASSIFICATION OF:

a. REPORT	b. ABSTRACT	c. THIS PAGE	17. LIMITATION OF ABSTRACT	18. NUMBER OF PAGES	19a. NAME OF RESPONSIBLE PERSON
U	U	U	U	64	Liu, David, Capt

19b. TELEPHONE NUMBER *(include area code)*
937-255-6565 x4542; david.liu@afit.edu

Standard Form 298 (Rev. 8–98)
Prescribed by ANSI Std. Z39.18